Delft University of Technology

Warm dust surface chemistry

H_2 and HD formation

Thi, W. F.; Hocuk, S.; Kamp, I.; Woitke, P.; Rab, Ch; Cazaux, S.; Caselli, P.

Important note
To cite this publication, please use the final published version (if applicable).
Please check the document version above.

Astronomy & Astrophysics

Warm dust surface chemistry

H$_2$ and HD formation

W. F. Thi[1], S. Hocuk[1,6], I. Kamp[2], P. Woitke[3,7], Ch. Rab[4,1], S. Cazaux[5], and P. Caselli[1]

[1] Max Planck Institute for Extraterrestrial Physics, Giessenbachstrasse, 85741 Garching, Germany
[2] Kapteyn Astronomical Institute, University of Groningen, Postbus 800, 9700 AV Groningen, The Netherlands
   e-mail: kamp@astro.rug.nl
[3] SUPA, School of Physics & Astronomy, University of St. Andrews, North Haugh, St. Andrews, KY16 9SS, UK
[4] Institute for Astrophysics, Türkenschanzstr.17, 1180 Vienna, Austria
[5] Faculty of Aerospace Engineering, Delft University of Technology, Delft, The Netherlands
[6] CentERdata, Tilburg University, PO Box 90153, 5000 LE, Tilburg, The Netherlands
[7] Centre for Exoplanet Science, University of St Andrews, St Andrews, UK

ABSTRACT

Context. Molecular hydrogen (H$_2$) is the main constituent of the gas in the planet-forming disks that surround many pre-main-sequence stars. H$_2$ can be incorporated in the atmosphere of the nascent giant planets in disks. Deuterium hydride (HD) has been detected in a few disks and can be considered the most reliable tracer of H$_2$, provided that its abundance throughout the disks with respect to H$_2$ is well understood.

Aims. We wish to form H$_2$ and HD efficiently for the varied conditions encountered in protoplanetary disks: the densities vary from 10^4 to 10^{16} cm^{-3}; the dust temperatures range from 5 to 1500 K, the gas temperatures go from 5 to a few 1000 Kelvin, and the ultraviolet radiation field can be 10^7 stronger than the standard interstellar field.

Methods. We implemented a comprehensive model of H$_2$ and HD formation on cold and warm grain surfaces and via hydrogenated polycyclic aromatic hydrocarbons in the physico-chemical code PROtoplanetary DIsk MOdel. The H$_2$ and HD formation on dust grains can proceed via the Langmuir-Hinshelwood and Eley-Ridel mechanisms for physisorbed or chemisorbed H (D) atoms. H$_2$ and HD also form by H (D) abstraction from hydrogenated neutral and ionised PAHs and via gas phase reactions.

Results. H$_2$ and HD are formed efficiently on dust grain surfaces from 10 to ∼700 K. All the deuterium is converted into HD in UV shielded regions as soon as H$_2$ is formed by gas-phase D abstraction reactions. The detailed model compares well with standard analytical prescriptions for H$_2$ (HD) formation. At low temperature, H$_2$ is formed from the encounter of two physisorbed atoms. HD molecules form on the grain surfaces and in the gas-phase. At temperatures greater than 20 K, the encounter between a weakly bound H- (or D-) atom or a gas-phase H (D) atom and a chemisorbed atom is the most efficient H$_2$ formation route. H$_2$ formation through hydrogenated PAHs alone is efficient above 80 K. However, the contribution of hydrogenated PAHs to the overall H$_2$ and HD formation is relatively low if chemisorption on silicate is taken into account and if a small hydrogen abstraction cross-section is used. The H$_2$ and HD warm grain surface network is a first step in the construction of a network of high-temperature surface reactions.

Key words. astrochemistry – molecular processes – methods: numerical

1. Introduction

Molecular hydrogen is the most abundant molecule in virtually every interstellar environment from the Milky Way to high-redshift objects. Molecular mass estimates are uncertain because direct observations of H$_2$ are hampered by its homonuclear nature. In addition, the lowest pure-rotation transition of H$_2$ is not observable from the ground. H$_2$ is also important as one of the major coolants of the warm gas (Shull & Hollenbach 1978; Flower et al. 1986; Shaw et al. 2005; Hollenbach & Tielens 1999). In cold regions, the interactions of H$_2$ with cosmic rays initiate the efficient ion-neutral chemistry.

Protoplanetary disk masses derived from CO and isotopologue observations tend to give values that are lower than estimates from dust observations (Miotello et al. 2016; Thi et al. 2001). HD has been used to infer high gas masses in protoplanetary disks (Bergin et al. 2013; McClure et al. 2016). Detailed modelling of the H$_2$ and CO chemistry is required to determine protoplanetary disk masses.

Molecular hydrogen is mostly formed on grain surfaces and through H-abstraction of hydrogenated polycyclic aromatic hydrocarbons (Wakelam et al. 2017; Gould & Salpeter 1963; Vidali 2013) because the low density of most interstellar environments excludes H$_2$ formation by three-body reactions. When a hydrogen atom collides with the dust, it can weakly bind to the surface by the van der Waals forces (a few meV), the interaction is then of the physisorption type. It can also strongly bind to the surface by the covalent force (eV), and the interaction is called chemisorption. In cold molecular cloud conditions, the dust grains are mostly below 15 K, a temperature low enough for two weakly bound physisorbed hydrogen atoms to stay on the grain surfaces. The surface hydrogen atoms scan the surfaces, meet each other, and recombine into H$_2$. In regions with dust temperatures higher than 20 K such as at the surface of photodissociation regions, only chemisorbed hydrogen atoms can remain on the grain surfaces. Hydrogen atoms can also chemically attach to polycyclic aromatic hydrocarbons (PAHs) to form hydrogenated PAHs or to amorphous carbon grains to form

hydrogenated amorphous carbon. H_2 is subsequently formed by abstracting the hydrogen from those species (Duley 1996; Pirronello et al. 1999; Mennella et al. 1999).

To account for the wide range of physical conditions (densities, gas and dust temperatures, radiation field) that occurs in planet-forming protoplanetary disks (Dutrey et al. 2014; Woitke et al. 2016), many physico-chemical disk models have implemented the H_2 formation model of Cazaux & Tielens (2002, 2004) with an efficient H_2 formation on warm dust grains. The H_2 formation rate in the interstellar medium (ISM) is constrained by precise observations obtained by the Far Ultraviolet Spectroscopic Explorer (FUSE) satellite at low density (Gry et al. 2002) and by the near-infrared H_2 emissions for dense photodissociation regions (PDRs, Habart et al. 2004).

H_2 formation models mostly focus on specific environments. Detailed Monte-Carlo kinetic simulations have been used to model H_2 formation in the diffuse cloud environment (Chang et al. 2006; Iqbal et al. 2012, 2014). Hincelin et al. (2015) proposed a method to model H_2 formation on low temperature grain surfaces. Le Bourlot et al. (2012) implemented a detailed model of H_2 formation for photodissociation regions including Langmuir-Hinshelwood and Eley-Rideal mechanisms and Bron et al. (2014) studied H_2 formation on stochastically heated small grains. Boschman et al. (2015) considered PAHs as an efficient medium for H_2 formation.

We present in this paper an H_2 formation model on warm dust grains and on hydrogenated PAHs. We have not considered H_2 formation on carbonaceous grains, which will be included in a future study. The model was designed to model H_2 formation for a large variety of physical conditions as found in protoplanetary disks. The results are compared to the formation rates computed using semi-analytical H_2 formation formulations. Our model relies on a set of measured and theoretical data.

Experimental studies on H_2 formation have been performed on cold ($T_d < 20$ K) polycrystalline (Pirronello et al. 1997) and amorphous silicates (Katz et al. 1999; Perets et al. 2007; Vidali et al. 2007; He et al. 2011; Gavilan et al. 2012). Physisorption of atomic hydrogen proceeds without a barrier (Downing et al. 2013; Navarro-Ruiz et al. 2014). He et al. (2011) concluded that the desorption energy distribution of the newly-formed HD is much broader if HD forms on an amorphous rather than on a crystalline silicate surface. Other studies concentrate on the H_2 formation (Perets et al. 2005; Roser et al. 2002; Manicò et al. 2001) on amorphous water ice since water ice mantles cover most grains at $A_V \geqslant 3$ mag (Boogert et al. 2015).

Once on a grain surface, an atomic hydrogen can diffuse and meet another atom. H atom diffusion on amorphous ice has been studied experimentally (Matar et al. 2008; Masuda et al. 1998; Watanabe et al. 2010; Hama et al. 2012; Dupuy et al. 2016) and theoretically (Al-Halabi & van Dishoeck 2007; Veeraghattam et al. 2014). The encounter between two atoms results in the H_2 formation. This reaction occurs with no or a small activation barrier of $\sim$250 K (Navarro-Ruiz et al. 2014). This mechanism, which involves two adsorbed species, is called the Langmuir-Hinshelwood mechanism (Hama & Watanabe 2013). An adsorbed H-atom can also react with an impinging gas-phase H atom to form H_2 in the so-called Eley-Rideal process.

At dust temperatures above $\sim$20 K, the surface residence time of physisorbed H atoms is so low that H_2 is not produced efficiently anymore. Only chemisorbed atoms remain on the surfaces long enough for H_2 to form. The formation of chemisorption bonds on graphitic and silicate surfaces implies overcoming activation barriers (Jeloaica & Sidis 1999; Sha et al. 2005; Bonfanti et al. 2015; Goumans et al. 2009; Martinazzo &

Tantardini 2006). Theoretical works on the chemisorption of hydrogen atoms on silicate surfaces seem to show at first sight large discrepancies in the energy barrier and binding energy. Garcia-Gil et al. (2013) computed via a first-principle computation the interaction of H with the (010) surface of forsterite (Mg_2SiO_4). By overcoming an activation barrier, H can attach either to a shallow chemisorption (1880 K, 162 meV) site after overcoming a small barrier of 290 K (25 meV), or to a deep chemisorption site with an absorption energy of 7775 K (670 meV) and a barrier of 1880 K (162 meV). Oueslati et al. (2015) performed density functional calculations with different Mg-rich olivine nano-clusters and concluded that there is a distribution of chemisorption sites with binding energy ranging from 8000 up to 30 000 K, see also Kerkeni & Bromley (2013). They demonstrated a linear dependency (Bell-Evans-Polanyi principle) between the activation energy for chemisorption E_{act} and the binding energy (E_b) and found a relationship between the H_2 reaction barrier for the Langmuir-Hinshelwood mechanism and the binding energy, independent of silicate dust grain shape, size, crystallinity and composition. Different types of nano-crystals and crystal surfaces have different chemisorption sites. Oueslati et al. (2015) findings can explain the large range of binding and activation energies found in various researches (Goumans et al. 2009; Kerkeni & Bromley 2013; Navarro-Ruiz et al. 2014, 2015). H_2 formation via the encounter of a gas-phase H atom and a chemisorbed atom (Eley-Rideal process) proceeds without activation barrier (Navarro-Ruiz et al. 2015).

H_2 can also form by the abstraction of an H-atom from hydrogenated PAHs with a small or no activation barrier (Farebrother et al. 2000; Rutigliano et al. 2001; Bachellerie et al. 2007; Ivanovskaya et al. 2010; Hirama et al. 2004; Skov et al. 2014; Pasquini et al. 2016). The sticking of H-atoms on graphitic surfaces and PAHs is the first step in the H_2 formation process and has been studied since the 1960s (Sha et al. 2005; Bonfanti et al. 2015; Ferullo et al. 2016). Dumont et al. (2008) studied the H_2 formation with a kinetic Monte-Carlo model.

The paper is organised as follows: in Sect. 2 we describe our H_2 and HD formation model. The analytical H_2 formation models are presented in Sect. 3. In Sect. 3 we also describe the grid of cloud models and the standard DIANA model for the comparison between our model and the analytical formulations. The PROtoplanetary DIsk MOdel (ProDiMo) is described in Sect. 4. In Sect. 5 we present the results and a discussion in our grid of models and conclude in Sect. 6.

2. H_2 and HD formation model

The H_2 and HD formation model on cold and warm dust grains follow that of Cazaux & Tielens (2002, 2004). H_2 formation on grain surfaces should occur for a wide range of grain temperatures. The binding energies of physisorbed species are between few 100 K up to few 1000 K. Chemisorbed species have binding energies of few 10 000 K. We take H_2 formation on PAHs (Sect. 2.7) and in the gas-phase (Sect. 2.8) into account.

Surface chemistry concepts are reviewed in Bonfanti & Martinazzo (2016). We introduce our notations and the notion of pseudo-species. Chemisorption sites are modeled by a pseudo-element named *, whose total elemental abundance is set by the number density of surface sites and the number of available grain surfaces, which itself depends on the grain size distribution. The pseudo-element * has also a pseudo-species counterpart *. The pseudo-species do not migrate nor desorb. Atomic

hydrogen atoms (and deuterium atoms) can adsorb weakly on a physisorption site, hop to a neighboring site or attempt to overcome a barrier to reach a strongly bound chemisorption site. Atoms can also diffuse between chemisorption sites or go to a physiorption site if they can overcome the activation barriers.

H$_2$ and HD formation occur via the Langmuir-Hinshelwood (LH) and Eley-Rideal (ER) mechanisms on dust grains and PAHs for physisorbed and chemisorbed species.

We assume that each physisorption site is associated with a chemisorption site. The physisorbed atoms are designated by H# and D#. The model includes the most abundant gas- and surface-species as listed in Table D.3. A chemisorbed atom is assigned a star * in front of it. Chemisorbed H and D are thus called *H# and *D# respectively. The pseudo-elemental conservation reads $[*] + [*H\#] + [*D\#] = n_* + n_{*H\#} + n_{*D\#} = n_{\text{surf,chem}}$, where $n_{\text{surf,chem}} = 4\pi N_{\text{surf}} r^2 n_{\text{d}}$ is the number density of chemisorption sites (N_{surf} is the surface density of physisorption and chemisorption sites and is equal to 1.5×10^{15} cm^{-2}, $nb_{\text{site}} = 4\pi N_{\text{surf}} r^2$ is the number of adsorption sites per monolayer, r is the grain mean radius, and n_{d} is the number density of dust grains in cm^{-3}). We adopted a treatment by rate reactions since the densities in disks are high ($n_{\text{H}} > 10^4$ cm^{-3}). The main surface reactions are listed in Table D.2. Table F.1 lists the main variables used in this study.

2.1. Adsorption and sticking

Most of the processes in our model follow the work of Hasegawa et al. (1992). The first process is the adsorption and desorption of atomic hydrogen or deuterium from the grain surfaces. A gas-phase atom or molecule i (in this paper i = H, D, PAH, ...) adsorbs on a surface physisorption (unlimited number) or a chemisorption (limited number) site at the general rate

$$R_i^{\text{ads}} = 4\pi r^2 \bar{v}_i f_{\text{avail}} n_{\text{d}} S_i Q_{\text{Bell}}(a_i^{\text{act}}, E_i^{\text{act}}, T_{\text{g}}) \text{ s}^{-1}, \tag{1}$$

where $4\pi r^2$ in cm^2 is the grain surface area (r is the grain radius), $\bar{v}_i = (kT_{\text{g}}/(2\pi m_i)^{1/2}$ is the thermal speed in cm s^{-1}, n_{d} is the number density of dust grains in cm^{-3}, and S_i is the sticking coefficient. The fraction of available sites f_{avail} is unity for physisorption and equal to the fraction of unoccupied sites for chemisorption ($f_{\text{avail}} = n_*/n_{\text{surf,chem}}$). Q_{Bell} is the transfer function (see Sect. 2.1.2). The treatment of the physisorption and chemisorption differs. The sticking coefficient depends on the surface and type of adsorption (Jones & Williams 1985).

2.1.1. Physisorption

There is no activation energy for physisorption ($Q_{\text{Bell}} = 1$). Hollenbach & McKee (1979) proposed for the sticking coefficient of H the following formula

$$S_{\text{phys}}^{-1} = 1 + 0.4 \times \left(\frac{T_{\text{g}} + T_{\text{d}}}{100}\right)^{0.5}$$
$$+ 0.2 \times \frac{T_{\text{g}}}{100} + 0.08 \times \left(\frac{T_{\text{g}}}{100}\right)^2. \tag{2}$$

The adsorption rate on physisorption sites (Eq. (1)) simplifies to

$$R_i^{\text{gp}} = 4\pi r^2 v_i^{\text{th}} n_{\text{d}} S_{\text{phys}} \text{ s}^{-1}. \tag{3}$$

We assume that the number of physisorption sites per grain remains constant as the ice mantle grows and that the mean grain

radius r is not changed. The sticking of atomic hydrogen on water ice has been recently studied (Veeraghattam et al. 2014) while Chaabouni et al. (2012) computed the sticking coefficient of H and D atoms onto silicate surfaces.

2.1.2. Eley-Rideal chemisorption

In the precursor-mediated adsorption mechanism, an atom adsorbs first without barrier to a weak physisorption site. This atom can subsequently diffuse to a deeper chemisorption site with small activation barrier (#H + * → #H*). The direct mechanism involves the gas-phase hydrogen (deuterium) atoms impinging on the surface and overcoming directly the activation barrier ($E_i^{\text{gc}} > 1000$ K). Theoretical studies on these two mechanisms do not show an actual decrease of the activation barrier for silicate grains when the atom is already physisorbed (Navarro-Ruiz et al. 2014). The chemisorption is of C1-type whereby the H$_{\text{chem}}^+$ is bonded to an O anion and a negative charge is transferred to a nearby Mg cation (Kerkeni et al. 2017). We treat the formation of a chemisorption bond from an impinging gas-phase H-atom (D-atom) as an activated Eley-Rideal process with rate R_i^{gc}

$$R_i^{\text{gc}} = \sqrt{\frac{kT_{\text{g}}}{2\pi m_i}} \frac{Q_i^{\text{gc}}}{N_{\text{surf}}} n_* S_{\text{chem}} \text{ s}^{-1}, \tag{4}$$

with the Bell's rate being $Q_i^{\text{gc}} = Q_{\text{Bell}}(a_i^{\text{gc}}, E_i^{\text{gc}}, T_{\text{g}})$, N_{surf} is the number density of surface sites (in cm^{-2}), and n_* the number density of chemisorption sites (cm^{-3}). The probability to overcome an adsorption activation barrier for chemisorption is described by a tunnelling-corrected Arrhenius formula called Bell's formula (Bell 1980):

$$Q_{\text{Bell}}(a_i^{\text{gc}}, E_i^{\text{gc}}, T_{\text{g}}) = \frac{\beta \exp(-\alpha) - \alpha \exp(-\beta)}{\beta - \alpha}, \tag{5}$$

where

$$\alpha = E_i^{\text{gc}}/kT_{\text{g}}, \tag{6}$$

and

$$\beta = \frac{4\pi a_i^{\text{gc}}}{h} \sqrt{2m_i E_i^{\text{gc}}}. \tag{7}$$

m_i is the mass of the impinging species (m_{H} for H or m_{D} for D). a_i^{gc} is the width of the activation barrier assuming a rectangular-shaped barrier of height E_i^{gc}, and h is the Planck constant. The Bell's formula is non-dimensional and reduces to the thermal term when tunnelling does not occur ($a_i^{\text{gc}} \to \infty$). It has been used successfully to model gas-phase rates when direct tunnelling effects occur.

One can determine a temperature T_{q} below which the quantum tunnelling effect dominates by equating α with β for a general process with an activation barrier:

$$T_{\text{q}} = \left(\frac{E_{\text{act}}}{k}\right) \left(\frac{h}{4\pi a \sqrt{2mE_{\text{act}}}}\right) = 2.46243 \left(\frac{E_{\text{act}}}{a_{\text{Å}}^2 m_{\text{amu}}}\right)^{1/2}, \tag{8}$$

where E_{act} is the activation energy in Kelvin, $a_{\text{Å}}$ is the barrier width in Å, and m_{amu} is the mass of the tunnelling species in

atomic mass units. The assumed value of the barrier width $a_{\text{Å}}$ has a stronger impact on the species diffusion rate than the mass or diffusion energy, for which only the square root of the value counts, at low surface temperature.

The barrier width for H-atom (and D-atom) Eley-Rideal chemisorption is assumed to be 0.5 Å. The sticking coefficient S plays a major role at high dust temperature in controlling the chemisorption (Cazaux et al. 2011). Both sticking coefficients account for the effect of gas and dust temperatures.

The inverse of the surface density of sites N_{surf} is a typical surface site cross-section ($\sigma_{\text{surf,site}} = 1/N_{\text{surf}} \simeq 1/1.5 \times 10^{15}$ cm^2), $n_* = 4\pi r^2 f_{\text{avail}} n_{\text{d}} N_{\text{surf}} \leqslant n_{\text{surf,chem}}$ is the number density of unoccupied chemisorption sites. When the surface is covered by more than N_{layer} layers, the ER chemisorption rate is set to zero ($R_i^{\text{gc}} = 0$).

For chemisorption, we use the sticking coefficient of Cuppen et al. (2010) and Sha et al. (2005)

$$S_{\text{chem}} = \left(1 + 5 \times 10^{-2} \sqrt{T_{\text{g}} + T_{\text{d}}} + 1 \times 10^{-14} T_{\text{g}}^4\right)^{-1} \quad (9)$$

with temperatures in K. The adsorption rate coefficients are

$$dn_{\#,i}/dt = R_i^{\text{gp}} n_i \text{ cm}^{-3} \text{ s}^{-1} \quad (10)$$

for physisorption and

$$dn_{*,i}/dt = R_i^{\text{gc}} n_i \text{ cm}^{-3} \text{ s}^{-1} \quad (11)$$

for Eley-Rideal chemisorption.

2.2. Desorption

An adsorbed species can thermally desorb, or desorb after the absorption of a UV photon, or after a cosmic ray has crossed the grain and deposited some energy. Desorption can be an activated process and is endothermic. The desorption energy is defined as

$$E_i^{\text{des}} = E_i^{\text{b}} + E_i^{\text{des,act}} \text{ erg.} \quad (12)$$

For physisorption, which is non dissociative, there is no barrier ($E_i^{\text{des,act}} = 0$) and the desorption and binding energy E_i^{b} are equal. The binding energy E_i^{b} is in principle not a single value but follows a distribution of values. Breaking of a chemisorption bond involves an activation energy equal to the chemisorption activation energy. The thermal desorption rate is

$$R_i^{\text{cg,th}} = \nu_{0,i} Q_{\text{Bell}}(a_i^{\text{des,act}}, E_i^{\text{des,act}}, T_{\text{d}}) e^{-E_i^{\text{b}}/kT_{\text{d}}} \text{ s}^{-1}. \quad (13)$$

The frequency $\nu_{0,i}$ is given by the formula for a rectangular barrier of height E_i^{b}

$$\nu_{0,i} = \sqrt{\frac{2N_{\text{surf}} E_i^{\text{b}}}{\pi^2 m_i}}. \quad (14)$$

We derived a frequency $\nu_{0,i}$ of $(1-10) \times 10^{12}$ Hz assuming a surface site density of $N_{\text{surf}} = 1.5 \times 10^{15}$ sites cm^{-2}. Only desorption from chemisorption sites are activated $Q_{\text{Bell}}(a_i^{\text{des,act}}, E_i^{\text{des,act}}, T_{\text{d}}) = Q_i^{\text{cg}} = Q_i^{\text{gc}}$. For desorption from physisorption sites $Q_{\text{Bell}}(a_i^{\text{des,act}}, E_i^{\text{des,act}}, T_{\text{d}}) = 1$, thus

$$R_i^{\text{pg,th}} = \nu_{0,i} e^{-E_i^{\text{b}}/kT_{\text{d}}} \text{ s}^{-1}. \quad (15)$$

The total desorption rate for species i includes cosmic-ray hit induced desorption and is assumed to follow a first-order desorption process. It reads for the physisorbed species

$$R_i^{\text{des,pg}} = R_i^{\text{pg,th}} + R_i^{\text{pg,ph}} + R_i^{\text{pg,CR}} \text{ s}^{-1}, \quad (16)$$

and for the chemisorbed species

$$R_i^{\text{des,cg}} = R_i^{\text{cg,th}} + R_i^{\text{cg,ph}} + R_i^{\text{cg,CR}} \text{ s}^{-1}. \quad (17)$$

The desorption for species i reads

$$dn_i/dt = R_i^{\text{des,pg}} n_i^{\text{act}} + R_i^{\text{des,cg}} n_{*,i} \text{ cm}^{-3} \text{ s}^{-1}. \quad (18)$$

For physisorbed species the concentration of active surface species i is

$$\begin{aligned} n_i^{\text{act}} &= n_{\#,i} & \text{if } n_{\#,\text{tot}} \leqslant nb_{\text{site}} n_{\text{d}} \\ &= n_{\#,i}(N_{\text{act}}/N_{\text{layer}}) & \text{if } n_{\#,\text{tot}} > nb_{\text{site}} n_{\text{d}}, \end{aligned} \quad (19)$$

where the number of physisorbed layers on a dust grain is $N_{\text{layer}} = n_{\#,\text{tot}}/(n_{\text{d}} nb_{\text{site}})$. $nb_{\text{site}} = 4\pi r^2 N_{\text{surf}}$ is the number of adsorption sites per monolayer and $n_{\#,\text{tot}} = \sum_i n_{\#,i}$ is the total number density of physisorbed species and N_{surf} is the number of sites per monolayer. N_{act} is the number of chemically physisorption active layers and this is a free parameter of the model. The standard value used in our models for N_{act} is two. $n_{*,i}$ is the number density of chemisorbed species i. All chemisorbed species can desorb since we restrict the maximum number of chemisorption layers to one.

Photodesorption is accounted for either through a factor that scales with the interstellar UV field (0D model) or using the actual computed UV field obtained by detailed radiative transfer and photodissociation cross-sections (2D disk models). The photodesorption rate of physisorbed species i is given by

$$R_i^{\text{pg,ph}} = \pi r^2 \frac{n_{\text{d}}}{n_{\text{act}}} Y_i \chi F_{\text{Draine}} \text{ s}^{-1}, \quad (20)$$

where Y_i is the photo-desorption yield, $\chi F_{\text{Draine}} = 1.9921 \times 10^8$ photons cm^{-2} s^{-1} is the local UV energy density computed from continuum radiative transfer (e.g., Woitke et al. 2009). We assume that photodesorption affects chemisorbed species the same way with rate $R_i^{\text{cg,ph}}$.

Cosmic-ray induced desorption follows the treatment of Hasegawa & Herbst (1993).

$$R_i^{\text{pg,CR}} = f(70 \text{ K}) R_i^{\text{pg,th}}(70 \text{ K}) \frac{\zeta_{\text{CR}}}{5 \times 10^{-17}} \text{ s}^{-1}, \quad (21)$$

where ζ_{CR} is the cosmic ray ionisation rate of H$_2$, $f(70 \text{ K}) = 3.16 \times 10^{-19}$ the "duty-cycle" of the grain at 70 K and $R_i^{\text{des,th}}(70 \text{ K})$ the thermal desorption rate for species i at temperature $T_{\text{d}} = 70$ K. The adopted value for $f(70 \text{ K})$ is strictly valid only for 0.1 μm grains in dense molecular clouds. Explosive desorption is not considered and will be included in future works (Ivlev et al. 2015). The dust temperature after a cosmic-ray hit is not high enough to desorb thermally a species in a chemisorption site.

2.3. Thermal and tunnelling surface diffusion

On grain surfaces the diffusive movement of H atoms from one site to another site occurs either by thermal hopping when there is sufficient energy to overcome the energy barrier or by tunnelling. Diffusion can be viewed as a random walk process. Atoms on a physisorption site can hop to another such site or to a deeper chemisorption site after overcoming an activation barrier (Barlow & Silk 1976; Leitch-Devlin & Williams 1984; Tielens & Allamandola 1987). An H-atom in a chemisorption site needs to overcome the energy difference between a physisorption and a chemisorption site in addition to the activation barrier in order to move to a physisorption site (Aronowitz & Chang 1980). We use again the Bell's formula to model the surface diffusion tunnelling effects

$$R_i^{\text{diff,th}} = \nu_{0,i} Q_i^{\text{diff}}(a_i^{\text{diff}}, E_i^{\text{diff}}) e^{-\Delta E_{ij}/kT_d}/nb_{\text{site}} \text{ s}^{-1}. \tag{22}$$

The factor Q_i^{diff} is the Bell formula (Eq. (5)) with

$$\alpha = E_i^{\text{diff}}/kT \tag{23}$$

and

$$\beta = \frac{4\pi a_i^{\text{diff}}}{h} \sqrt{2mE_i^{\text{diff}}}. \tag{24}$$

ΔE_{if} is the binding energy difference between the two adsorption sites

$$
\begin{aligned}
\Delta E_{if} &= 0 && \text{if } E_i^{\text{b}} \leqslant E_f^{\text{b}}, \\
\Delta E_{if} &= E_i^{\text{b}} - E_f^{\text{b}} && \text{otherwise.}
\end{aligned} \tag{25}
$$

Thus $\Delta E = 0$ for hopping between two physisorption sites or between two chemisorption sites. m is the mass of the diffusing species. α corresponds to the thermal diffusion (hopping) while β refers to the quantum tunnelling. The diffusion time t_i^{diff} is the inverse of R_i^{diff}. The surface diffusion rates for species i are defined as the combination of thermal, tunnelling and cosmic-ray induced diffusion

$$R_i^{\text{diff}} = R_i^{\text{diff,th}} + R_i^{\text{diff,CR}} \text{ s}^{-1}, \tag{26}$$

where the cosmic-ray induced diffusion rate is (Hasegawa & Herbst 1993; Reboussin et al. 2014)

$$R_i^{\text{diff,CR}} = f(70\,\text{K})\, R_i^{\text{diff,th}}(70\,\text{K})\, \frac{\zeta_{\text{CR}}}{5 \times 10^{-17}} \text{ s}^{-1}. \tag{27}$$

An atom bound at a physisorption site can diffuse to another physisorption site, desorb, or land on the chemisorption site associated with the current physisorption site (Cazaux & Tielens 2002, 2004). This view is valid when the current physisorption site is related to a silicate or carbonaceous surface, for example when the surface has fewer than a monolayer of ice. In denser regions, multi-layer ice mantle can be built rapidly. When the grain has one or more monolayers, the H-atom can only physisorb on the water ice mantle. In this case we assume that a physisorbed H/D-atom can still diffuse through the bulk of the ice mantle but at a lower diffusion rate than on the ice mantle surface and overcome the barrier to land on an available chemisorption site. The diffusion rates state that bulk diffusion is permitted so that as the ice mantle grows, the number of sites available for scanning also increases, independently of the assumed number of active layers. The reactions compete

explicitly with the desorption processes (thermal, cosmic-ray induced, and photodesorption). Their respective rates concern the active species. The process is formally represented as

$$\text{H\#} + * \rightarrow *\text{H\#}, \tag{28}$$

and

$$\text{D\#} + * \rightarrow *\text{D\#}. \tag{29}$$

The diffusion of species i is restricted to the physisorption active layers similar to the desorption

$$\text{d}n(i)/\text{d}t = R_i^{\text{diff}} n_i^{\text{act}}(i) \text{ cm}^{-3} \text{ s}^{-1}. \tag{30}$$

An alternative interpretation of our assumption is that the average diffusion rate for all the species on the surface and in the bulk is lower by a factor $N_{\text{act}}/N_{\text{layer}}$ when there is more than one monolayer.

2.4. The rate equation treatment

Since we focus on H_2 and HD formation in dense cold and warm regions, we adopted the rate equation treatment for the surface chemistry.

2.4.1. Langmuir-Hinshelwood reactions

The Langmuir-Hinshelwood surface reaction prescription follows the implementation of Hasegawa et al. (1992). The surface reaction rate coefficient k_{ij} (cm^3 s^{-1}) between surface species i and j with respective number density n_i and n_j is the probability of reaction per encounter (κ_{ij}) times the rate of encounter between the two species scanning the surface:

$$k_{ij} = \kappa_{ij}(R_i^{\text{diff}} + R_j^{\text{diff}})/n_d \text{ cm}^3 \text{ s}^{-1}, \tag{31}$$

where κ_{ij} is the probability for the reaction to occur upon encounter between species i and j after both have diffused on the grain mantle, R_i^{diff} and R_j^{diff} (s^{-1}) are the diffusion rates for species i and j, and n_d (cm^{-3}) is the number density of dust grains. We assume that the newly-formed H_2 molecules desorb immediately because of the high exothermicity of the reaction. The probability for the reaction to occur follows a competition between association of the two species, modeled by the Bell formulation to account for thermal crossing and tunnelling of potential activation barrier, and diffusion (Bonfanti & Martinazzo 2016; Garrod & Pauly 2011; Ruaud et al. 2016)

$$\kappa_{ij} = \frac{Q_{\text{Bell}}(a_{ij}^r, E_i^{\text{act}})}{Q_{\text{Bell}}(a_{ij}^r, E_i^{\text{act}}) + P_i^{\text{diff}} + P_j^{\text{diff}}}, \tag{32}$$

where a_{ij}^r is the width of the barrier and E_i^{act} the activation barrier height (energy) and $P_i^{\text{diff}} = R_i^{\text{diff}}/\nu_{0,i}$. The mass used in the Bell formula is that of the lighter species. When no competition is accounted for, the probability is

$$\kappa_{ij}' = \nu_{0,i} Q_{\text{Bell}}(a_{ij}^r, E_i^{\text{act}}). \tag{33}$$

For barrierless reactions, $\kappa_{ij} = 1$ and $\kappa_{ij}' = 1$, and the rate becomes

$$k_{ij} \simeq (R_i^{\text{diff}} + R_j^{\text{diff}})/n_d \text{ cm}^3 \text{ s}^{-1}. \tag{34}$$

When $E_i^{\text{act}} \ll E_i^{\text{diff}}$ and without tunnelling effects, $\kappa_{ij} \to 1$ and the rate approaches the diffusion-limited rate

$$k_{ij} \simeq (R_i^{\text{diff}} + R_j^{\text{diff}})/n_d \ \text{cm}^3 \ \text{s}^{-1}, \tag{35}$$

while without competition the rate is

$$k'_{ij} = \nu_{0,i} Q_{\text{Bell}}(a_{ij}^r, E_i^{\text{act}})(R_i^{\text{diff}} + R_j^{\text{diff}})/n_d \ \text{cm}^3 \ \text{s}^{-1}. \tag{36}$$

In that case, $k_{ij} \gg k'_{ij}$. On the other hand, when $E_i^{\text{act}} \gg (E_i^{\text{diff}}, E_j^{\text{diff}})$, the diffusion terms ($R_i^{\text{diff}}$ and R_j^{diff}) dominate and cancel out in the rate coefficient (since the diffusion terms are present as numerator and denominator), and the rate becomes

$$k_{ij} \simeq \nu_{0,i} Q_{\text{Bell}}(a_{ij}^r, E_i^{\text{act}})/n_d \ \text{cm}^3 \ \text{s}^{-1}, \tag{37}$$

with again $k_{ij} \gg k'_{ij}$. The diffusion is so fast that the reactants are always in the situation where the recombination (association) can occur.

The barrier for H diffusion from a physisorption site to another one in Kelvin is between 256 K (Kuwahata et al. 2015) and 341 K (Congiu et al. 2014) whereas the barrier for H_2 formation is 250 K or less (Navarro-Ruiz et al. 2014). We adopted a barrierless H_2 recombination between two physisorbed H atoms.

At $10 < T_d < 20$ K and assuming a comparable diffusion and association (reaction) activation energy and weak photodissociation, the probability of the reaction becomes $\kappa_{ij} \simeq 1/3$. At low temperature ($T_d < 10$ K), thermal processes become insignificantly slow and both the diffusion and reaction rates are dominated by tunnelling. Diffusion tunnelling of H-atoms has a large barrier width of ~ 3.9 Å compared to ~ 0.5 Å for the reaction barrier (Limbach et al. 2006) such that the reactive tunnelling rate dominates at $T_d < 10$ K and the probability of reaction becomes $\kappa_{ij} \simeq 1$. Therefore, the H_2 formation rate below 20 K by recombination of the physisorbed H-atoms is diffusion limited even if a small barrier exists. We do not restrict H_2 formation by recombination of physisorbed H-atoms (LH mechanism) even when the surface is covered by a layer of physisorbed H-atoms (Gavilan et al. 2012).

2.4.2. Eley-Rideal reactions

According to the semi-equilibrium theory, the probability of a gas-phase radical recombining with an atom located in an adsorption site is equal to the probability of the gas atom directly impinging on the occupied site multiplied by the probability of the gas atom having enough kinetic energy to overcome the reaction barrier, if any, with the possibility to tunnel through the barrier. Due to the long-range attractive potential, the impinging species has an energy of $1/2 k T_g + E_i^{\text{b}}$ relative to the surface species (E_i^{b} is the binding energy). Part of this energy can be used to overcome a reaction barrier.

Laboratory and theoretical works suggest that the formation of H_2 via the ER process is barrierless (or has a very small barrier) both on silicate and carbonaceous surfaces. The Eley-Rideal formation of H_2 from an impinging H on a physisorbed or chemisorbed H-atom has a rate of

$$R_{H_2}^{\text{gp}} = \sqrt{\frac{k T_g}{2\pi m_H}} \frac{1}{N_{\text{surf}}} n_{H\#} = 2.425 \times 10^{-12} \sqrt{T_g} n_{H\#} \ \text{s}^{-1} \tag{38}$$

and

$$R_{H_2}^{\text{gc}} = \sqrt{\frac{k T_g}{2\pi m_H}} \frac{1}{N_{\text{surf}}} n_{*H\#} \ \text{s}^{-1}. \tag{39}$$

For HD, the rate is composed of two terms, one is the rate when a gas phase atom hits a chemisorbed D-atom and the second when a D-atom hits a chemisorbed H atom. The rate $R_{H_2}^{\text{gc}}$ is zero when there is more than N_{layer} layers of ice. If this occurs the water-ice mantle shields the chemisorbed H-atoms from being directly hit by a gas-phase atom.

2.5. Diffusion-mediated chemisorption

As the direct Eley-Rideal chemisorption is hampered by the presence of the water ice mantle below the water sublimation temperature (between 90 and 150 K depending on the gas density), chemisorption mostly occurs after an H-atom has diffused through the mantle and reached the interface between the mantle and the refractory surface. The diffusion rate in the bulk is decreased by the total number of ice layers. This is an extremely simple method to model a slower diffusion in the ice mantle compared to the diffusion at the ice surface. At the interface, the H-atom can overcome the barrier to chemisorption. The rate for this reaction is

$$R_{H\#}^{\text{pc}} = \kappa_{H\#}^{\text{pc}} R_{H\#}^{\text{diff}} (n_*/n_d) \ \text{s}^{-1}. \tag{40}$$

This rate should be compared to the thermal-dominated desorption rate of the physisorbed H-atom

$$R_{H\#}^{\text{pg}} = \nu_{\text{pg}} e^{-E_{H\#}^{\text{b}}/kT_d} \ \text{s}^{-1}. \tag{41}$$

In the thermal regime ($T_d > T_q = 78$ K), the lowest activation barrier for chemisorption is $E_{H\#}^{\text{act}} \sim 900$–1000 K on silicate (Oueslati et al. 2015) compared to a diffusion energy of $\simeq 406$ K (Perets et al. 2007) and an adsorption energy of $\simeq 510$ K. The diffusion-mediated chemisorption rate is reaction-limited

$$R_{H\#}^{\text{pc}} = \nu_{H\#}^{\text{pc}} Q_{H\#}^{\text{pc}} (n_*/n_d) \simeq \nu_{H\#}^{\text{pc}} e^{-E_{H\#}^{\text{act}}/kT_d} (n_*/n_d). \ \text{s}^{-1} \tag{42}$$

The activation barrier to form H_2 from the encounter of a physisorbed and a chemisorbed atom is the same as the barrier to form a chemisorption bond because both processes involve the breaking of the H chemical bond to the surface. The rate per gas volume is

$$dn_{*H\#}/dt = R_{H\#}^{\text{pc}} n_H^{\text{act}} \ \text{cm}^{-3} \ \text{s}^{-1}. \tag{43}$$

The reverse mechanism is a chemisorbed H-atom escaping the deep well to reach a physisorption site $R_{*H\#}^{\text{cp}}$. The formation of H_2 can happen after a H-atom (H#) hops from a physisorption site to a site occupied by a chemisorbed H-atom with number density $n_{*H\#}$. The rate is

$$R_{H\#,*H\#} = R_{H\#}^{\text{diff}} (n_{*H\#}/n_d) \ \text{s}^{-1}. \tag{44}$$

2.6. Reactions involving PAHs

PAHs are not formed or destroyed in our chemical network and only exchange charges with other positively-charged species (for example H^+, He^+, Mg^+, Fe^+, C^+, Si^+, S^+, HCO^+, ...) or can be hydrogenated (PAH-H_x, PAH$^+$-H_x, PAH-H_xD, PAH$^+$-H_xD, $x = 0, 1,...,18$). The ionised PAH-H_xs can recombine with a free electron. Chemical reaction rates involving PAHs are highly uncertain. Most of the rates are extrapolations from a few existing laboratory or theoretical rates and are discussed in Appendix B.

Table 1. PAH successive hydrogenation energy barriers ($E_{\text{PAH}-\text{H}_x,\text{H}}^{\text{act}}/k$) in Kelvin.

Hydrogenation level	Outer edge	Edge	Center	Ref.
PAH-H	116	1740	2553	[a]
	692			[b]
	324			[c]
PAH-H$_2$	348	2669	3365	[a]
	0			[b]
	0			[c]
PAH-H$_3$	348			[b]
	533			[c]
PAH-H$_4$	0			[b]
	0			[c]
PAH-H$_5$	0			[b]
	742			[c]
PAH-H$_6$	0			[b]
	0			[c]
PAH-H$_7$	0			[b]
	406			[c]
PAH-H$_8$	0			[b]
	0			[c]
PAH-H$_9$	**348**			[c]
PAH-H$_{10}$	**0**			[c]
PAH-H$_{11}$	**603**			[c]
PAH-H$_{12}$	**0**			[c]
PAH-H$_{13}$	**382**			[c]
PAH-H$_{14}$	**0**			[c]
PAH-H$_{15}$	**382**			[c]
PAH-H$_{16}$	**0**			[c]
PAH-H$_{17}$	**452**			[c]
PAH-H$_{18}$	**0**			[c]

Notes. The adopted values are shown in bold face.

References. [a] Cazaux et al. (2016) for PAH cations; [b] Rauls & Hornekær (2008); [c] Boschman et al. (2015), the values are for coronone C$_{24}$H$_{12}$.

2.7. H$_2$ and HD formation on neutral and cationic PAHs

Experimental and theoretical studies on neutral hydrogenated PAHs (called here PAH-H$_x$, with $x = 1, 2, ..., 18$) suggest that H$_2$ can form through barrierless Eley-Rideal abstractions (Bauschlicher 1998; Mennella et al. 2012; Rauls & Hornekær 2008; Thrower et al. 2012). Morisset & Allouche (2008) computed quantum dynamically the sticking of an H atom on a graphite surface.

The H$_2$ formation proceeds in two steps. The first step is the hydrogenation of the PAHs or ionised PAHs, followed by H-abstraction. The adopted PAH is the large compact circumcoronene (C$_{54}$H$_{18}$), which has a peri-condensed stable structure (Tielens et al. 1987). Although the carbon backbone fragmentation efficiency upon absorption of a UV photon increases with the degree of hydrogenation (Wolf et al. 2016), we modeled hydrogenated PAHs up to PAH-H$_x$ with $x = 18$ equal to the number of edge carbon for the circumcoronene.

We adopted a cross section of 1.1 Å^2 per reactive carbon atom for radiative hydrogen association (Boschman et al. 2015)

together with a barrier E_i^{act}

$$k_{\text{PAH}-\text{H}_x,\text{H}} = 2.78 \times 10^{-11} \sqrt{\frac{T_g}{300}} N_C Q_{\text{Bell}}(E_{\text{PAH}-\text{H}_x,\text{H}}^{\text{act}}) \text{ cm}^3 \text{ s}^{-1},$$

(45)

where $Q_{\text{Bell}}(E_{\text{PAH}-\text{H}_x,\text{H}}^{\text{act}})$ is a Bell's formula (Eq. (5)). This means that we consider that H-tunnelling is possible. It is clear that hydrogenation of neutral PAHs is an activated process because the formation of a C-H bond requires a rehybridisation (sp2 to sp3) of the carbon orbitals. Various authors (Rauls & Hornekær 2008; Karlicky et al. 2014; Allouche et al. 2006; Ferullo et al. 2016; Klose 1992) quote a value of $E_{\text{PAH}-\text{H}_x,\text{H}}^{\text{act}}/k = 692$ K (0.06 eV). Other studies (Sha et al. 2005) found a barrier of 2321 K (0.2 eV). Aréou et al. (2011) found experimental evidence of a barrier.

Cazaux et al. (2016) and Rauls & Hornekær (2008) have studied the successive PAH hydrogenation barriers. The barrier energies depend on the type of attachment sites (outer edge site, an edge site, or a center site). Table 1 provides a summary of the values present in the literature. Computations (Rauls & Hornekær 2008) suggest that the barrier vanishes for high levels of hydrogenation. Boschman et al. (2015) modeled the PAH hydrogenation with alternate high and low barriers. We adopted the series of barrier energies from Boschman et al. (2015). Low energy barriers are central to permit H$_2$ formation at intermediate dust temperatures ($T_d = 20$–100 K) when the chemisorption on silicate grains may be inefficient.

De-hydrogenation of PAH-H$_x$ ($x \geq 1$), occurs mostly by photodissociation. The photodissociation threshold for hydrogenated circumcoronene (E_{th}) is equal to the binding energy (Andrews et al. 2016). Computations of the binding energies depend on whether H is chemisorbed to an edge carbon (C$_{\text{edge}}$) or not (C$_{\text{graph}}$), see Ferullo et al. (2016) or Rasmussen (2013). When it is attached to a C$_{\text{graph}}$ atom, the binding energy is $\sim$0.6 eV. An atom attached to an edge carbon is more strongly bound (1–2 eV). The binding energy was found for H and D on graphite to be 0.6 (6963 K) and 0.95 eV (11024 K, Zecho et al. 2002a and Ferro et al. 2003). The chemisorption site for an H atom, which is located on the top of a C$_{\text{graph}}$ carbon atom, has an energy of 0.57 eV (6847 K) for coronene C$_{24}$H$_{12}$ (Jeloaica & Sidis 1999) and weak binding sites with 0.040 eV (464 K) may exist (Ma et al. 2011). Haruyama & Watanabe (2011) found a binding energy of pyrene C$_{16}$H$_{10}$ of 0.6 eV. Ferullo et al. (2016) used an improved density function theory model and computed for a chemisorption binding on an edge carbon a binding energy of 2 eV for anthracene. In this study the adsorption (binding) energies of an H-atom on a C$_{\text{edge}}$ atom of a PAH are taken from Klærke et al. (2013) and Bauschlicher & Ricca (2014). For circumcoronene, the binding energy E_0 of an extra H-atom in a C-H bound is $\sim$1.4 eV (16250 K).

The unimolecular thermal dissociation rate of a PAH-H$_x$ at an effective temperature T_e follows an Arrhenius approximation to the Rice-Ramsperger-Kassel-Marcus (RKKM) model (Jochims et al. 1994)

$$R_{\text{PAH}-\text{H}_x,\text{T}_e} = R_0(T_e) \exp\left(-E_0/kT_e\right) \text{ s}^{-1},$$

(46)

where T_e is an effective temperature for a PAH with N_C carbon atoms upon absorption of a photon of energy $h\nu$ in eV (Tielens 2005):

$$T_e \simeq 2000 \left(\frac{h\nu}{N_C}\right)^{0.4} \left(1 - 0.2\left(\frac{E_0}{h\nu}\right)\right).$$

(47)

The pre-exponential factor $R_0(T_e) = (kT_e/h) \exp(1 + (\Delta S/R))$ s^{-1} (Reitsma et al. 2014), where ΔS is the entropy change assumed to be 55.6 J K^{-1} mol^{-1} (Ling & Lifshitz 1998) and R is the gas constant.

Unimolecular dissociation competes with relaxation by the emission of infrared photons with a typical rate R_{IR} of 1 s^{-1}. The yield for photodissociation for $h\nu > E_0$ reads

$$Y_{PAH-H_x,UV} = \frac{R_{PAH-H_x,T_e}}{R_{PAH-H_x,T_e} + R_{IR}}. \tag{48}$$

The yield is zero for $h\nu < E_0$. The yield is used together with the PAH cross-section (Draine & Li 2001; Li & Draine 2001) and the local UV field spectrum to compute the actual photodissociation rate.

PAHs and hydrogenated PAHs can exchange IR photons with the dust grains and reach an average temperature T_{PAH}. In radiative thermal equilibrium T_{PAH} is equal to the dust grain temperature T_d in the optically thick midplane of protoplanetary disks (Woitke et al. 2016). Hydrogenated PAHs can undergo thermal unimolecular dissociation with the rate

$$R_{PAH-H_x,therm} = R_0(T_{PAH}) \exp(-E_0/kT_{PAH}) \text{ s}^{-1}. \tag{49}$$

An impinging H-atom can abstract the dangling H from a hydrogenated PAH-H_x to form H_2 (or PAH-H_xD to form HD) via a barrierless Eley-Rideal mechanism (Rauls & Hornekær 2008; Bauschlicher 1998). Cuppen & Hornekær (2008) model the H_2 formation by abstraction from hydrogenated graphite using the kinetic Monte-Carlo technique.

The cross-section for this reaction is 0.06 Å^2 per reactive carbon atom (Mennella et al. 2012) for neutral PAHs

$$k_{PAH-H_x,H} = 1.5 \times 10^{-12}(T_g/300)^{1/2} N_C^{reac} \text{ cm}^3 \text{ s}^{-1}. \tag{50}$$

$N_C^{reac} = x$ for PAH-H_x when the rate scales with the number of extra hydrogens attached to the PAH. A small barrier ($\sim$10 meV, or $\sim$115 K) may be present, but we choose to neglect it (Casolo et al. 2009). Petucci et al. (2018) computed a high energy of 1150 K for the barrier. Zecho et al. (2002b) found that the D abstraction on low D-covered graphite bombarded with H-atoms proceeds with a cross-section of up to 17 Å^2 (and 4 Å^2 at high coverage). Eley-Rideal cross sections around 4 Å^2 have been also computed by Pasquini et al. (2016) using the quasi-classical trajectory method. The cross-sections do not show isotopic dependencies. Therefore, we adopted the same cross-section for H and D formation on hydrogenated PAHs using the cross-section measured in the experiments on amorphous carbon (a:C-H) by Mennella et al. (2012), which is however much lower than the values measured by Zecho et al. (2002b) or comptued by Pasquini et al. (2016). Duley (1996) adopted a cross section of 10 Å^2. On the other extreme, Skov et al. (2014) estimated an extremely low cross-section of 0.01 Å^2. We tested the effect of choosing a higher abstraction cross-section in Appendix C.

PAHs and hydrogenated PAHs can be ionised at low A_V and ionisation competes with photodissociation. A lower value of 0.02 Å^2 has been reported by Oehrlein et al. (2010). The hydrogenation of PAH cations

$$PAH^+ + H \rightarrow (PAH - H)^+ \tag{51}$$

proceeds without activation barrier or with a small barrier. Cazaux et al. (2016) computed a small barrier of 116 K (0.01 eV) for the first hydrogenation of coronene cation, consistent with the

value of Hirama et al. (2004). The rate is quasi-independent on the size of the PAH (Demarais et al. 2014; Snow et al. 1998). We adopt therefore a size-independent rate

$$k_{PAH-H_x^{n+},H} = 2 \times 10^{-10} \left(\frac{T_g}{300}\right)^{-1.5} Q_{Bell}(E^{act}_{PAH-H_x^{n+},H}) \text{ cm}^3 \text{ s}^{-1}, \tag{52}$$

with $E^{act}_{PAH-H_x^{n+},H}$=116 K. We further assume that the photodissociation of ionised hydrogenated PAHs follow the same rate as for the neutral PAHs.

H-abstraction reaction with cationic hydrogenated PAHs is a barrierless ion-neutral reaction. Therefore, the rate should be in the order of magnitude of a Langevin rate. We choose to use the scaling law of Montillaud et al. (2013)

$$k_{(PAH-H_x)^{n+}} = 1.4 \times 10^{-10} \left(\frac{N_H}{12}\right) \left(\frac{N_C}{24}\right)^{-1} \text{ cm}^3 \text{ s}^{-1}, \tag{53}$$

where N_H and N_C are the number of hydrogen and carbon atoms that constitute the PAH respectively and $n+$ is the charge of the PAH. The standard interstellar abundance of PAHs is 3×10^{-7} (Tielens 2005). In protoplanetary disks, a fraction f_{PAH} is still present. The H_2 formation efficiency depends on the charge of the PAH and hydrogenated PAHs. The recombination of PAH-H^+ follows the same rate as for PAH$^+$ apart that the recombination is dissociative PAH $- H^+ + e^- \rightarrow$ PAH $+$ H.

Hydrogen atoms can also physisorb on PAHs. The H_2 formation can be theoretically more efficient than formation from chemsisorbed H atoms for graphite (Casolo et al. 2009). We have not considered H_2 formation from photodissociation of PAHs (Castellanos et al. 2018a,b). H diffusion can compete with desorption Borodin et al. (2011). In our model we assumed that H-atoms are too strongly bound for an efficient diffusion to another site for chemisorption.

2.8. H_2 gas-phase formation and destruction

We incorporated in our H_2 and HD formation model the major formation and destruction routes for H_2. Gas-phase H_2 reactions have been discussed by Glover (2003) and Galli & Palla (1998). The formation occurs via H^-, whose electron can be ejected, carrying with it the excess heat of formation of 4.8 eV

$$\begin{aligned} H + e^- &\rightarrow H^- + h\nu, \\ H^- + H &\rightarrow H_2 + e^-, \end{aligned} \tag{54}$$

with rate for the second reaction taken from Launay et al. (1991) and Martinez et al. (2009). For H^+, the reactions are

$$\begin{aligned} H + H^+ &\rightarrow H_2^+ + h\nu, \\ H_2^+ + H &\rightarrow H_2 + H^+. \end{aligned} \tag{55}$$

In both cases, the first step is a slow radiative recombination reaction. The hydrogen anions and cations are destroyed by mutual neutralisation (Moseley et al. 1970)

$$H^+ + H^- \rightarrow H + H, \tag{56}$$

and H^+ can recombine with an electron

$$H^+ + e^- \rightarrow H, \tag{57}$$

or the electron can be photodetached

$$H^- + h\nu \rightarrow H + e^-. \tag{58}$$

Protons are formed by charge exchange with He^+ or by ionisation by X-rays or cosmic rays. They can recombine or exchange the charge with a species X with ionisation potential lower than 13.6 eV

$$H^+ + e^- \rightarrow H + h\nu, \tag{59}$$

or the electron can be photodetached

$$H^+ + X \rightarrow H + X^+. \tag{60}$$

At densities $>10^8$ cm^{-3}, three body reactions become important and the third body carries the excess heat of formation in form of kinetic energy (Palla et al. 1983)

$$\begin{aligned} H + H + H &\rightarrow H_2 + H, \\ H + H + H_2 &\rightarrow H_2 + H_2. \end{aligned} \tag{61}$$
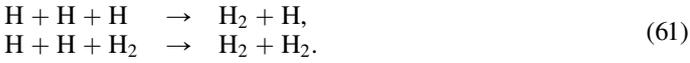
The rate coefficient for the first reaction is controversial (Forrey 2013a,b; Jacobs et al. 1967; Abel et al. 2002; Flower & Harris 2007; Palla et al. 1983) as it is a prime path to form H_2 in the early Universe. Rates for the second reaction have been measured by Trainor et al. (1973) or modeled by Whitlock et al. (1974) and Schwenke (1988, 1990).

At very high gas densities and temperatures, collision-induced dissociations (collider reactions) can occur (Ohlinger et al. 2007).

2.9. H_2 destruction by dissociative chemisorption

At high gas temperatures, H_2 impinging on bare silicate grain surfaces can dissociatively chemisorb

$$H_2 + * \rightarrow *H\# + H\#, \tag{62}$$

where we adopted a barrier height of 5802 K (Song & Xu 2016) with the rate given by Eq. (4). The dissociative chemisorption of H_2 on PAH edges proceeds as

$$H_2 + PAH - H_x \rightarrow PAH - H_{x+1} + H, \tag{63}$$
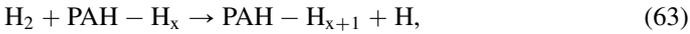
with a barrier height of 3481 K (Diño et al. 2004).

2.10. HD formation and destruction

HD formation occurs both on grain surfaces, by abstraction of hydrogenated PAHs and by deuterium substitutions in the gas-phase (Cazaux & Spaans 2009). H_2 has a zero-point energy of 3135.5 K (2179.3 ± 0.1 cm^{-1}) and HD of 2719.7 K (1890.3 ± 0.2 cm^{-1}) resulting in an energy difference of $\Delta E^{H_2-HD} = 415.8$ K (Irikura 2007). The formation of HD occurs also in the gas-phase where exchange reactions can be efficient (Watson 1973; Brown & Rice 1986). Gas phase HD formation reactions have been discussed in the context of a dust free or low-metallicity early Universe (Stancil et al. 1998; Galli & Palla 1998; Cazaux & Spaans 2009), a cold molecular cloud by Roueff et al. (2007) and for PDR regions by Le Petit et al. (2002). The lower zero-point energy of the deuterated species translates into larger reaction activation energies. The radiative association

$$H + D \rightarrow HD + h\nu \tag{64}$$

has an extremely low rate of 8×10^{-27} cm^{3}s^{-1} at 100 K (Stancil & Dalgarno 1997). In the gas-phase, HD can be formed efficiently at high temperature by the substitution reaction once H_2 has been formed (Mitchell & Le Roy 1973; Sun et al. 1980; Garrett & Truhlar 1980; Simbotin et al. 2011) by the reaction

$$H_2 + D \rightleftarrows HD + H, \tag{65}$$

which has a barrier of 3820 K. The backward reaction is endothermic by 420 K. We adopted an endothermicity of 415.8 K. The ion-neutral reaction

$$H_2 + D^+ \rightleftarrows HD + H^+ \tag{66}$$

behaves unexpectly with temperature (Smith et al. 1982; Honvault & Scribano 2013; González-Lezana et al. 2013; Lara et al. 2015) and follows a Langevin rate of $\sim 2.1 \times 10^{-9}$ cm^3 s^{-1} ($k = 2.05 \times 10^{-9} (T/300)^{0.2417} \exp(-3.733/T_d)$ cm^3 s^{-1}). The backward reaction is endothermic by 462 K. D^+ is formed from H^+ via

$$H^+ + D \rightleftarrows H + D^+, \tag{67}$$

with an endothermicity of 41 K (Watson 1976). In regions of low ionisation (low cosmic ray flux), this route may become inefficient. At low temperature, the rates of neutral-neutral reactions are negligible without tunnelling effects. Forward deuteration fractionation reactions are reversible with the forward reaction favoured because of the difference in zero-point energies.

H_2 and HD can be photodissociated and a self-shielding factor applies to both molecules with H_2 being much more shielded than HD (Le Petit et al. 2002; Thi et al. 2010).

2.11. Adopted data

The conclusions from our modelling depend on the choice of the molecular data. It is believed that amorphous silicates can react with H (D) atoms more effectively and/or rapidly than crystalline silicates because they are thermodynamically unstable. Silicate surfaces show a distribution of chemisorption sites with binding energies ranging from ~ 1000 to $\sim 20\,000$ K (Oueslati et al. 2015). The activation energy to overcome the barrier and chemisorb follows the Bell-Evans-Polanyi principle. As the dust grain temperature increases, chemisorption sites with deeper potential are open so that we assume a binding energy of $35 \times T_d$, knowing that the typical desorption occurs at $E^b_{*H\#}/30$ K (Luna et al. 2017)

$$E^b_{*H\#}/k = 35 \times T_d \text{ K}, \tag{68}$$

with $\min(E^b_{*H\#}/k) = 10\,000$ K and $\max(E^b_{*H\#}/k) = 25\,000$ K. We adopted a simple relation between the activation energy E^{act}_* and the binding energy $E^b_{*H\#}$

$$E^{act}_*/k = E^b_{*H\#}/k - 9100 \text{ K}, \tag{69}$$

which gives an activation energy of $E^{act}_H/k = 900$ K for a binding of $E^b_{*H\#}/k = 10\,000$ K. The lowest activation energy is consistent with the value of Cazaux & Tielens (2002). Both paths to form a chemisorbed H have the same barrier energy ($E^{gc}_H = E^{pc}_{H\#} = E^{act}_H$). The barrier energy for the reaction between a physisorbed and a chemisorbed H-atom is $E_{H\#,*H\#} = E^{act}_H$. There is no barrier for the Eley-Rideal H_2 formation ($E_{H,*H\#} = 0$) and the barrier

Table 2. Surface molecular data for physisorption processes.

Surface	E_i^{b}/k (K)	E_i^{diff}/k (K)	a_{db} (Å)
H atom			
Amorph. silicate	510 [a]	406 [a]	3.8 [a]
Amorph. ice	650 [b]	341 [c]	3.9 [c]
	607 [d]	516 [d]	
Poly-crystalline ice		256 [e]	
D atom			
Amorph. sillicate	569 [a]	406 [a]	3.8 [a]
Amorph. ice	708 [b,f]	341 [g]	
Amorph. ice	665 [d]	415.8 [d]	
		255 [h]	
Poly-crystalline ice		267 [e]	

References. [a] Exp.: Perets et al. (2007); [b] theor.: Al-Halabi & van Dishoeck (2007); [c] exp.: from a fit to the data from Congiu et al. (2014); [d] exp.: Perets et al. (2005); exp.: [e] Kuwahata et al. (2015) ; [h] exp.: Matar et al. (2008);

is $E_{*\mathrm{H}\#,*\mathrm{H}\#} = 2E_{\mathrm{H}}^{\mathrm{act}}$ for H_2 formation from two chemisorbed atoms because it implies the breaking of two chemisorption bonds. For physisorption, there is also a variety of experimental and theoretical energies, which are summarised in Table 2. The diffusion barrier and the desorption energies for H atoms on amorphous silicate were taken from Perets et al. (2007). Hama et al. (2012) showed that there are many physisorption sites with a central energy of 22 meV. Ásgeirsson et al. (2017) have theoretically shown that a distribution of desorption (32–77 meV or 371–894 K) and diffusion (1–56 meV or 11–650 K) energies exists for H in an amorphous water ice matrix with a linear dependency of $E_{\mathrm{H}\#}^{\mathrm{diff}} = 0.68\, E_{\mathrm{H}\#}^{\mathrm{b}}$. The theoretical results confirm the experiments where more than one energy has been found (Hama et al. 2012). Ásgeirsson et al. (2017) provide a possible explanation on the discrepancy between different experimental results (Manicò et al. 2001; Perets et al. 2005; Hornekær et al. 2003; Matar et al. 2008). At low H-coverage, H is mostly adsorbed on the deep sites, while at high coverage the deep sites are occupied and H atoms reside in shallower sites. The distribution in binding energies is narrower for crystalline ice.

The greater mass of a D atom compared to a H atom results in a smaller zero-point-energy and therefore in a larger binding energy. The binding energy for a D atom is $\simeq 58$ K (5 meV) higher than the value for a H atom (Le Petit et al. 2009). The diffusion energy barrier is not affected by the difference in zero-point-energy and $E_{\mathrm{D}\#}^{\mathrm{diff}} = E_{\mathrm{H}\#}^{\mathrm{diff}}$ since the zero-point-energy is accounted for in both the initial and final site.

Our choice of energies for physisorption is guided by: (1) we adopt a unique relatively high binding energy of $E_{\mathrm{p}}^{\mathrm{des}}/k = E_{\mathrm{H}\#}^{\mathrm{b}}/k = 600$ K whether H is attached on amorphous silicate or on amorphous water ice corresponding to a low coverage situation; (2) we adopt the scaling law of Ásgeirsson et al. (2017) and obtain $E_{\mathrm{H}\#}^{\mathrm{diff}}/k = 408$ K; (3) $E_{\mathrm{D}\#}^{\mathrm{des}}/k = E_{\mathrm{p}}^{\mathrm{des}}/k + 58 = 658$ K; (4) $E_{\mathrm{D}\#}^{\mathrm{diff}} = E_{\mathrm{H}\#}^{\mathrm{diff}} = 408$ K. The chemisorption binding energies for HD are increased by 58 K from the values for H_2.

We illustrate the application of the Bell's formula to the tunnelling diffusion of physisorbed H-atoms. The physisorbed H-atom diffusion behaviour on cold grain surfaces is discussed in detail in Congiu et al. (2014). In the Bell's formula, E_i^{diff} is
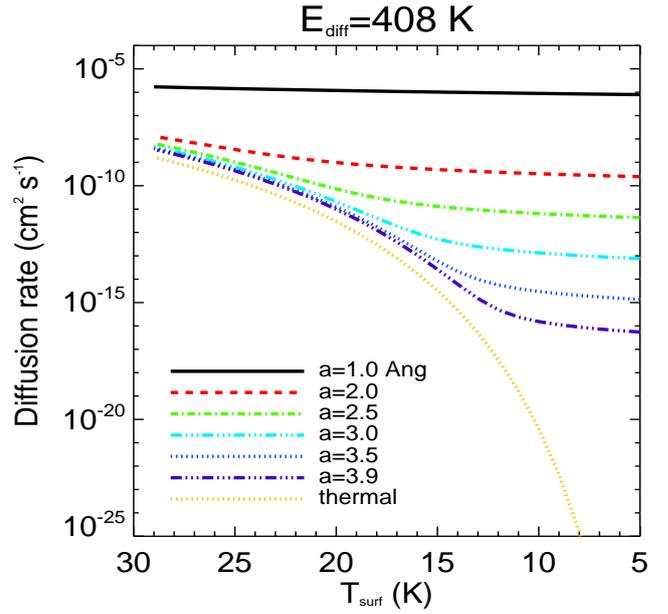
Fig. 1. Atomic hydrogen grain surface diffusion rate as function of the surface temperature for different values of the barrier width a in Å. In our model, we choose a value of 3.9 Å. The thermal diffusion rate is also shown.

the surface thermal diffusion in erg. For physisorbed H-atoms, we adopt a diffusion energy of 408 K. The barrier width to tunnelling $a_{\mathrm{H}\#}^{\mathrm{pp}}$ on amorphous water ice surface is found by matching the experimental data (Congiu et al. 2014) and a reasonable value is $a_{\mathrm{H}\#}^{\mathrm{pp}} = 3.9 \times 10^{-8}$ cm (3.9 Å). h is the Planck constant in erg s and m is the mass of the diffusing species in gram. The surface diffusion rate for a H-atom $k_i^{\mathrm{diff}} = \nu_0 Q_i^{\mathrm{diff}}/N_{\mathrm{surf}}$ (cm^{-2} s^{-1}) is shown for different choices of the barrier width in Fig. 1. The figure also shows a purely thermal surface diffusion rate, which drops dramatically at low dust temperatures below T_q=11 K from Eq. (8).

3. Previous analytical H_2 formation models on silicate dust grains

3.1. Cazaux model

The standard analytical model for H_2 formation follows the model of Cazaux & Tielens (2002, 2004), which is based on the model of Hollenbach et al. (1971). The rate is

$$R_{\mathrm{H}_2}^{\mathrm{Cazaux}} \equiv \frac{1}{2}\, \varepsilon\, 4\pi r^2\, v_{\mathrm{H}}^{\mathrm{th}}(T_{\mathrm{g}})\, S_{\mathrm{H}}\, n_d \equiv \frac{1}{2} R_{\mathrm{H}}^{\mathrm{ads}}\ \mathrm{s}^{-1}, \tag{70}$$

where $v_{\mathrm{H}}^{\mathrm{th}} = (kT_{\mathrm{g}}/(2\pi m_{\mathrm{H}}))^{1/2}$ is the thermal relative velocity of the hydrogen atom, $4\pi r^2 n_{\mathrm{d}}$ is the total surface of the dust component per volume, S_{H} is the sticking coefficient, and ϵ is the recombination efficiency. The formula can be derived from the steady-state balance between formation and destruction of a physisorbed H-atom H#

$$\mathrm{d}n_{\mathrm{H}\#}/\mathrm{d}t = R_{\mathrm{H}}^{\mathrm{ads}} n_{\mathrm{H}} - R_{\mathrm{p}}^{\mathrm{des}} n_{\mathrm{p}} - 2k_{\mathrm{H}_2}^{\mathrm{pp}} n_{\mathrm{p}} n_{\mathrm{p}} = 0 \tag{71}$$

and the H_2 formation rate density is

$$(\mathrm{d}n_{\mathrm{H}_2}/\mathrm{d}t)_{\mathrm{form}} = k_{\mathrm{H}_2} n_{\mathrm{p}} n_{\mathrm{p}}\ \mathrm{cm}^{-3}\ \mathrm{s}^{-1}. \tag{72}$$

At low temperatures and low UV field, we can neglect the desorption, and we obtain the formation rate density

$$(dn_{H_2}/dt)_{form} = \frac{1}{2} R_H^{ads} n_H \; cm^{-3} \; s^{-1}, \tag{73}$$

where n_H is the number density of atomic hydrogen in the gas (in cm^{-3}). The rate density is strictly speaking an upper limit since H atoms have to adsorb first. For HD formation, we follow the model described in Cazaux & Spaans (2009) and the rate assumes the same efficiency as for H_2.

3.2. Jura's empirical H_2 formation rate coefficient

The H_2 formation (Eq. (70)) can be rewritten to recover the standard rate for H_2 formation, which has been measured by Jura (1974, 1975a,b). The observed rate has been derived from observations obtained by the Copernicus satellite in diffuse clouds and confirmed by Gry et al. (2002) using FUSE observations. First we define the average number of dust grains as

$$n_d = \frac{1.386 \; amu \; n_{\langle H \rangle} \delta}{(4/3)\pi \rho_d r^3} \; cm^{-3}, \tag{74}$$

which can be approximated by

$$n_d \approx 1.83 \times 10^{-15} \, n_{\langle H \rangle} \left(\frac{\mu m^3}{r_{\mu m}^3} \right) \left(\frac{\delta}{0.01} \right) \; cm^{-3}, \tag{75}$$

where δ is the dust-to-gas mass ratio assumed to be 0.01 and the total gas number density is $n_{\langle H \rangle} = n_H + 2n_{H_2}$ and $r_{\mu m}$ is the grain radius in micron. We have assumed a silicate mass density ρ_d of 3.0 g cm^{-3}. The abundance of Helium is 0.096383, giving an extra mass to the gas of 0.386 to the hydrogen nuclei mass. For an average grain radius r of 0.1 μm and an efficiency of unity, we can find

$$R_{H_2} = 4.18 \times 10^{-18} S_H \sqrt{T_g} (0.1 \; \mu m/r_{\mu m}) n_{\langle H \rangle} \; s^{-1}. \tag{76}$$

The formation rate does not explicit dependent on the dust temperature. The implicit assumption ($\varepsilon = 1$) is that all adsorbed H-atom will eventually leave the grain as H_2. The H_2 formation rate coefficient for a gas at 80 K as found in the diffuse interstellar medium, $r_{\mu m} = 0.1$, and a sticking coefficient of unity, is

$$k_{H_2} = 3.74 \times 10^{-17} \; cm^3 \; s^{-1}, \tag{77}$$

which is consistent with the values found by Gry et al. (2002) between 3.1×10^{-17} and 4.5×10^{-17} cm^3 s^{-1}. They confirmed the earlier results of Jura (1975a), who found an H_2 formation rate coefficient of 3.0×10^{-17} cm^3 s^{-1}. Therefore, Jura's H_2 formation rate coefficient is compatible with the highest possible rate for H_2 formation on silicate dust grains. The empirical H_2 formation rate coefficient relies on a detailed knowledge of the H_2 photodissociation rate in the clouds.

4. ProDiMo chemical models

PRODIMO is a code built to model the gas and dust grain physics and chemistry (Woitke et al. 2009, 2016; Kamp et al. 2010). It has been used to model disk Spectral Energy Distributions (SEDs, Thi et al. 2011), water deuteration chemistry (Thi et al. 2010) CO rovibrational emissions including UV-fluorescence (Thi et al.

Table 3. Cloud model parameters.

Parameter	Symbol	Values
Gas density	$n_{\langle H \rangle}$	2×10^4 cm^{-3}
Temperature	$T_d = T_g$	10–700 K
Extinction	A_V	10
Strength of interstellar UV	χ^{ISM}	1
Cosmic ray H_2 ionisation rate	ζ_{CR}	1.7×10^{-17} s^{-1}
Mean grain radius	r	10^{-5} cm
Dust-to-gas mass ratio	δ	0.01
PAH abundance rel. to ISM	f_{PAH}	1

Notes. $\chi^{ISM} = 1$ is the ISM Draine UV field. $f_{PAH} = 1$ corresponds to a PAH abundance of 3×10^{-7}.

Table 4. Cloud models.

| #	Model	Physi-sorption	Chemi-sorption	Formation on PAHs
1	MC-ANALYTIC			
2	MC-PHYS	$\checkmark$		
3	MC-PHYS-CHEM-PAH	$\checkmark$	$\checkmark$	$\checkmark$

2013), and many *Herschel* observations from the GASPS key programme (Dent et al. 2013). X-ray physics are implemented (Aresu et al. 2011, 2012; Meijerink et al. 2012; Rab et al. 2018). A detailed discussion of the different physics and their implementations are given in the articles listed above. Here we summarise the main features. In our chemical modelling, we included 116 gas and ice species, and PAHs. Self-shielding against photodissociation for H_2 and HD is taken into account. Reaction rate coefficients that are not explicitly discussed in this paper are taken from UMIST2012 (McElroy et al. 2013). The adsorption energies are mixed from various sources (Aikawa et al. 1996; Garrod & Herbst 2006, and UMIST2012 McElroy et al. 2013). The network was complemented by reactions relevant to high temperature conditions (Kamp et al. 2017). We used the chemistry solver in the PRODIMO code in a zero-dimensional model (see Table 3 for the basic choice of parameters). Further modelling in the context of protoplanetary disks will be reported in subsequent articles. The assumptions are $T_d = T_g$, a fixed UV field strength and extinction A_V for the zero-dimensional model. We expanded the so-called small disk chemical network by including the species required to model H_2 and HD formation (see Table D.1). Only relevant surface and gas-phase chemical reactions are included, and they are listed in Tables D.2 and D.3. The latter table lists reactions with singly-hydrogenated PAHs. Similar reactions with multi-hydrogenated PAHs are used in the modelling but are not shown. The results of runs with multiply-hydrogenated PAHs are shown in Appendix C. The elemental abundances are taken from Kamp et al. (2017) and in addition the adopted deuterium elemental abundance is 1.5×10^{-5} (Linsky et al. 1995).

5. Results and discussions

5.1. Analytical H_2 formation efficiency

The H_2 formation rate at all temperatures without considering the Eley-Rideal processes reads

$$(dn_{H_2}/dt)_{LH} = k^{pp} n_p n_p + k^{pc} n_p n_c + k_{H_2}^{cc} n_c n_c. \tag{78}$$
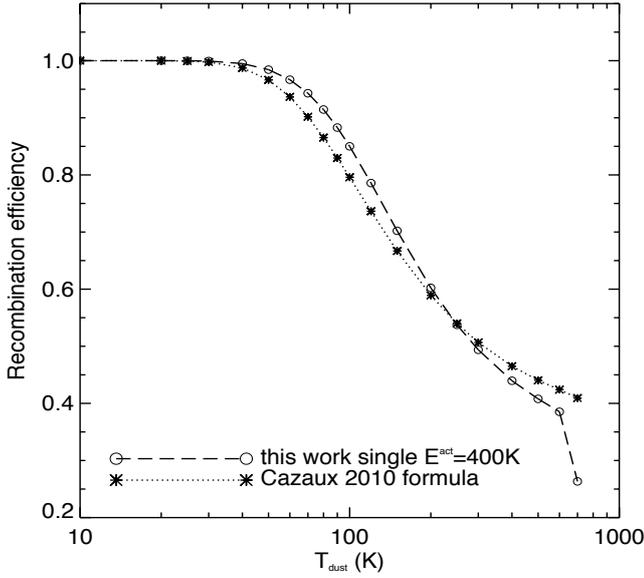
Fig. 2. Comparison between the analytic H$_2$ formation efficiency using the formula from Cazaux & Tielens (2004) with the 2010 update (the binding energy for physisorbed H-atom $E_{H_p} = 600$ K, and the saddle point $E_S = E_{H_p} - E^{pc} = 200$ K, with E^{pc} being the activation energy to overcome to go from a physisorption site to a chemisorption site) and our numerical code for a zero-dimensional cloud model.

We assume that $E_{H\#,*H\#} = E_{H\#}^{pc} = \min(E^{sil}) = E_{H\#}^{sil} = 1000$ K and the barrier width $a_{H\#}^{pc}$ is 1 Å and obtain $T_q \simeq 78$ K using Eq. (8). Here we did not study the effects of different values for the barrier width. In addition, the shape of the barrier has been assumed to be rectangular although the use of most realistic barrier profiles may affect the results (Taquet et al. 2012). Knowing that $n_{surf,chem} = 4\pi N_{surf} r^2 n_d \simeq n_* + n_c$ (some chemisorbed sites can be occupied by D atoms), for T_d below 78 K, we can use the quantum tunnelling transfer function in the recombination-limited approximation ($E_{H\#}^{sil} \gg E_p^{des}$)

$$\alpha_{pc} \simeq \nu_{H\#}^{pc} \exp\left(-\frac{4\pi a_{H\#}^{pc}}{h}\sqrt{2m_H E_{H\#}^{sil}},\right) \text{ s}^{-1}. \qquad (79)$$

For all $T_d < 78$ K, $\alpha_{pc} \gg R_p^{des}$. When the rate coefficient is dominated by the chemisorption barrier term, the diffusion-chemisorption rate coefficient for $T_d > 78$ K is

$$k_{H\#}^{pc} = \nu_{H\#}^{pc} e^{-E_{H\#}^{pc}/kT_d}/n_d n b_{site} \text{ cm}^3 \text{ s}^{-1}. \qquad (80)$$

The surface-mediated H$_2$ formation rate coefficient is in the thermal regime

$$k_{H\#,*H\#} \simeq \nu_{H\#,*H\#} e^{-E_{H\#,*H\#}/kT_d}/n_d n b_{site} \text{ cm}^3 \text{ s}^{-1}. \qquad (81)$$

The surface-mediated chemisorption processes rate becomes

$$\alpha_{pc} = k_{H\#}^{pc} n_* + k_{H\#,*H\#} n_c$$
$$\simeq \nu_{H\#}^{sil} e^{-E_{H\#}^{sil}/T_d}\left(n_{surf,chem}/n_d\right)/n b_{site} \text{ s}^{-1}, \qquad (82)$$

which arranges to

$$\alpha_{pc} \simeq \nu_{H\#}^{sil} e^{-E_{H\#}^{sil}/kT_d} \text{ s}^{-1}. \qquad (83)$$

In the thermal regime,

$$\frac{R_p^{des}}{\alpha_{pc}} \simeq \frac{\nu_p^{des} e^{-E_p^{des}/kT_d}}{\nu_{H\#}^{sil} e^{-E_{H\#}^{sil}/kT_d}}, \qquad (84)$$

which rearranges into

$$\frac{R_p^{des}}{\alpha_{pc}} \simeq \sqrt{\frac{E_p^{des}}{E_{H\#}^{sil}}} e^{-\left(E_p^{des} - E_{H\#}^{sil}\right)/kT_d}. \qquad (85)$$

In the diffusion-limited regime ($E_{H\#}^{sil} \ll E_p^{des}$), the ratio becomes

$$\frac{R_p^{des}}{\alpha_{pc}} \simeq \sqrt{\frac{E_p^{des}}{E_{H\#}^{diff}}} e^{-\left(E_p^{des} - E_{H\#}^{diff}\right)/kT_d}. \qquad (86)$$

The change of chemisorbed H-atom reads

$$dn_c/dt = k^{pc} n_p (n_* - n_c) - R_c^{des} n_c - 2k_{H_2}^{cc} n_c^2. \qquad (87)$$

In steady-state, this equation becomes

$$k^{pc} n_p (n_{surf,chem} - 2n_c) - R_c^{des} n_c - 2k_{H_2}^{cc} n_c^2 = 0, \qquad (88)$$

which is a second degree equation in n_c. The solution is

$$n_c = 2\alpha_{pc} n_p /$$
$$\left(-(R_c^{des} + 2k_{H\#}^{pc} n_p) + \sqrt{(R_c^{des} + 2k_{H\#}^{pc} n_p)^2 + 8k_{H_2}^{cc}\alpha_{pc} n_p}\right), \qquad (89)$$

where $k_{H\#}^{pc} n_p n_{surf,chem} = \alpha_{pc} n_p$. If the desorption of chemisorbed H-atoms can be neglected, the H$_2$ formation rate becomes

$$dn_{H_2}/dt \simeq \frac{1}{2} k_{H\#}^{pc} n_p n_*. \qquad (90)$$

Since $n_p = R_H^{ads} n_H/(\alpha_{pc} + R_p^{des})$, this can be re-written as

$$dn_{H_2}/dt \simeq \frac{1}{2}\left(1 + \frac{R_p^{des}}{\alpha_{pc}}\right)^{-1} R_H^{ads} n_H. \qquad (91)$$

The H$_2$ formation efficiency has been derived by Cazaux & Tielens (2002, 2004) using a different model

$$\epsilon = \left(1 + \frac{R_p^{des}}{\alpha_{pc}}\right)^{-1} \xi, \qquad (92)$$

with $R_p^{des} = \beta_{H_p}$ and ξ the correction factor at high temperatures, which accounts for the H atoms desorbing from chemisorption sites. Recent developments have shown that a layer of H$_2$ does not prevent the further formation of more H$_2$; thus we can neglect the first term in the parentheses in the formula of Cazaux & Tielens (2004). Both analytical efficiencies are shown in Fig. 2. Our curve has been obtained with a unique physisorption to chemisorption site activation energy of 400 K, which corresponds to a saddle point energy E_s of 200 K for Cazaux's formula. Despite the differences in the treatment of many processes (presence of chemisorption sites, diffusion-mediated versus direct transfer from a physisorption site to an
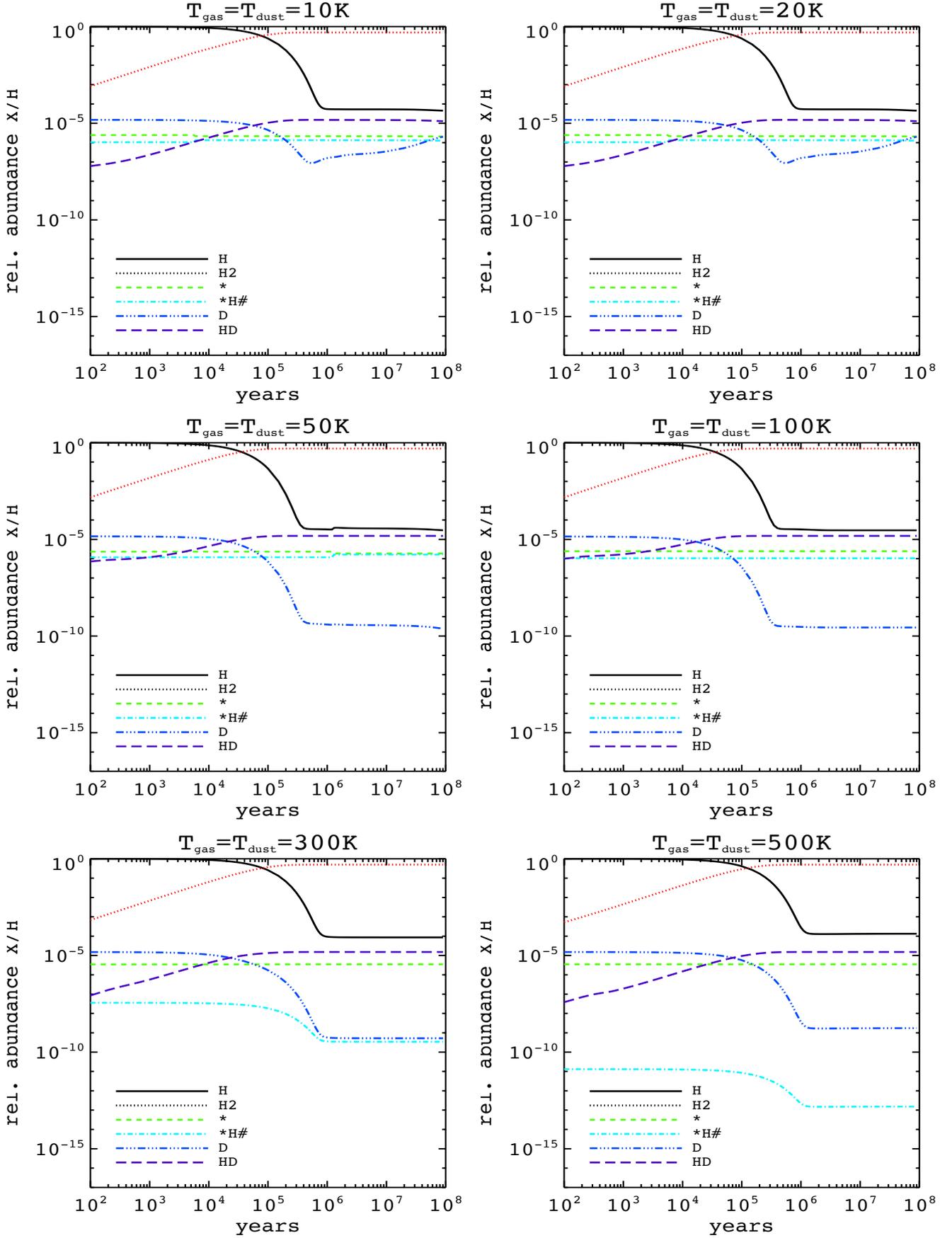
Fig. 3. H, H$_2$, D, HD, and physisorbed H as function of time using the surface chemistry model with physisorbed and chemisorbed species and a unique physisorption to chemisorption activation energy of 400 K. *First row, from left to right*: models at 10 and 20 K; *second row*: models at 50 and 100 K. *Bottom row*: models at 300 and 500 K. The * symbol corresponds to the abundance of unoccupied chemisorption sites.
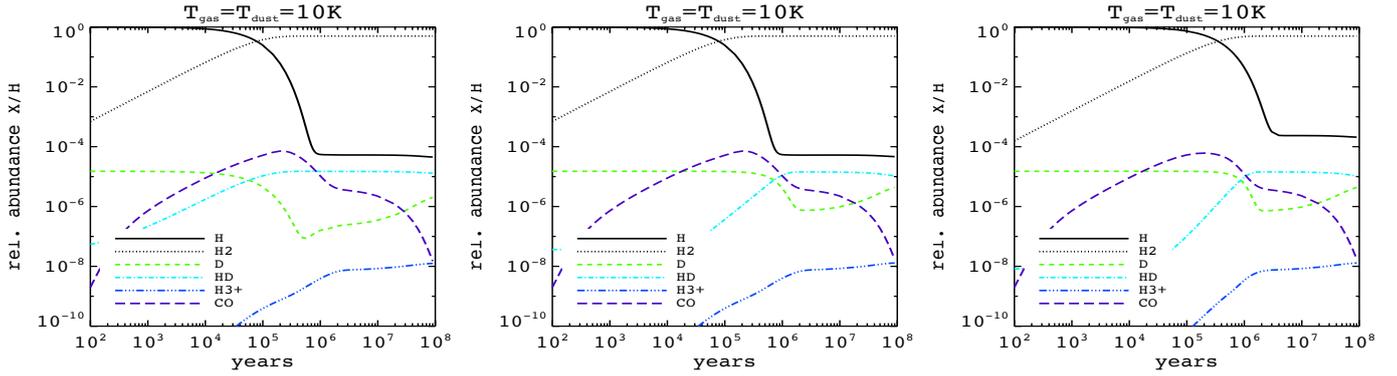
Fig. 4. H, H_2, D, HD, and physisorbed H as function of time at 10 K for three models of H_2 and HD formation. *Left model*: surface chemistry model without chemisorption species; *middle panel*: model with the analytical Cazaux formation model and *right panel*: utilises the H_2 formation model of Jura (1974, 1975a,b).
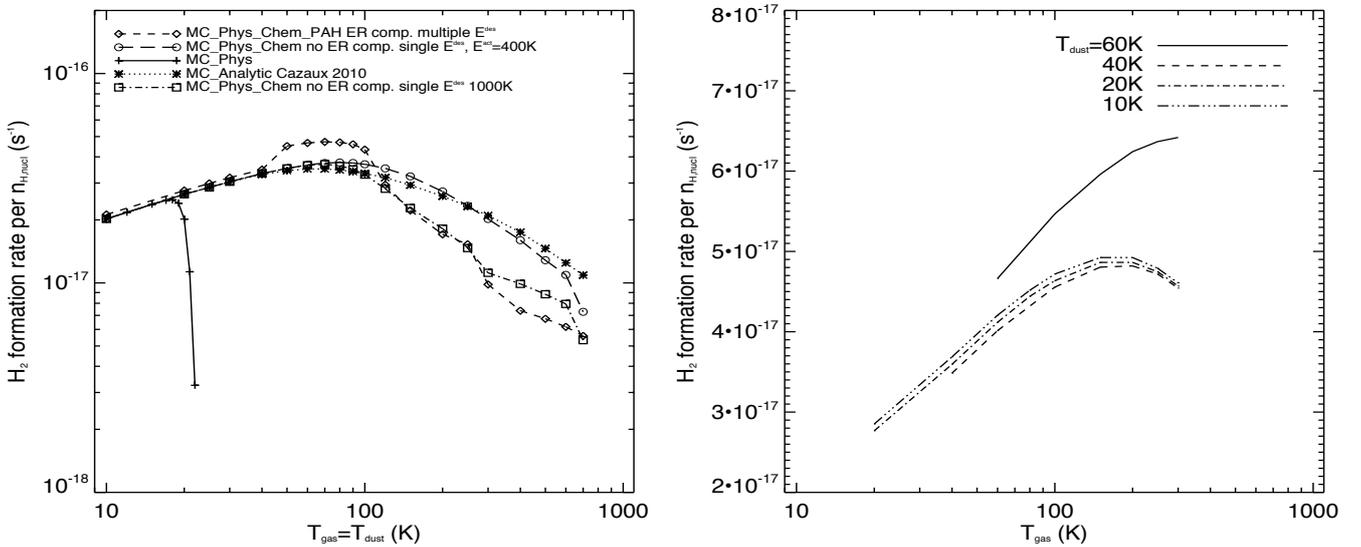
Fig. 5. Effective H_2 formation rate. *Left panel*: two H_2 formation models for a molecular cloud of $n_H = 10^4$ cm^{-3} and assuming $T_d = T_g$ (MC-ANALYTIC, MC-PHYS and MC-PHYS-CHEM-PAH). We also show the effect of competition diffusion-reaction rates (no compet. MC-PHYS-CHEM-PAH). *Right panel*: H_2 formation model MC-PHYS-CHEM-PAH when T_d and T_g can be different.

adjoining chemisorption site, "blocking" of chemisorption sites by ice layers, ...) between our model and the model from Cazaux & Tielens (2004), the agreement is remarkable for all temperatures. Differences appear in the upper end of the dust temperature range when the efficiency drops faster than in Cazaux's model due to the extra term $2k_{H\#}^{pc} n_p$ instead of only R_c^{des} when the efficiency is limited by the desorption only. As the efficiency remains relatively high even at 600 K, the actual H_2 formation rate is limited by the sticking coefficient at high dust temperatures (Cazaux et al. 2011). Part of the differences between the two efficiency curves can be ascribed to the use of different transmission functions for α_{pc} (see Fig. E.1).

5.2. Numerical models of molecular clouds

The abundances of H, H_2, D, HD, H physisorbed and chemisorbed on grain surfaces are shown in Fig. 3 for a zero-dimensional cloud model at several temperatures (10, 20, 50, 100, 300, and 500 K) with a single activation energy of 400 K from a physisorption to a chemisorption site at various grain temperatures. The complete conversion from H to H_2 is reached at all temperatures at $(1-2) \times 10^5$ yr. The number density of atomic

H plateaus at ~ 1 cm^{-3} after a few Myrs. At $T_d > 20$ K, HD reaches its maximum abundance faster than H_2.

Surface hydrogen is chemisorbed even at 10 K (see the top left panel of Fig. 3). Without chemisorption sites, the abundance of physisorbed H-atoms is 2.5 dex higher (see left panel of Fig. 4). This may affect the surface hydrogenation rates. The drop of the HD abundance for $t > 10$ Myrs is due to the strong fraction of HDO gas and HDO ice. The reason for this high chemisorption site occupancy is the large number of available chemisorption sites and the high surface diffusion rate.

We also run a series of models with only physisorption sites, a model with an activation barrier for chemisorption of 1000 K instead of 400 K, and a model with multiple barrier heights and Eley-Rideal formation processes included. The H_2 formation rate for a 0.1 micron grain is shown for the various models in the left panel of Fig. 5 for a few series of cloud models whose assumptions are summarised in Table 4. The rates were computed from the outcomes of the models themselves by determining at each temperature the time t_{H_2} that the model needs to convert 2/3 of the hydrogen atoms into molecules. The value of t_{H_2} is such that $n_{H_2} = n_H$. The formation rate R is computed as $R = 1/(t_{H_2} n_{\langle H \rangle})$.

Below 20 K, the H_2 formation is adsorption rate limited, independent of the actual H_2 formation rate on the grain surfaces as shown by the analytical treatment above. When the formation rate is low, the number density of H atoms on the surface increases. This is the case when the rate is lower after the formation of the H_2O ice layers. As expected, the desorption of H# above $\sim$20 K prevents H_2 formation. The computed H_2 formation rate differences between the Cazaux model and the surface chemistry model with a single barrier for chemisorption correspond to the differences seen in the analytical treatment (Fig. 2). H_2 formation is efficient up to $\sim$700 K (efficiency of 0.4), which corresponds to $\sim E_c^{\rm des}/30$ (Luna et al. 2017). Atomic D is only slightly more bound to the surface and will also form efficiently on grains up to $\sim$700 K. The building up of ice layers does not prevent surface H-atoms to reach the silicate surface and to adsorb on an empty chemisorption site. Both the diffusion and desorption rates decrease with an increasing number of ice layers.

The model with a single barrier of 1000 K for chemisorption shows a drop in efficiency above 100 K. It reflects the decrease in the $R_p^{\rm des}/\alpha_{\rm pc}$ ratio with a higher energy barrier. In the model with varying barrier energy and chemisorption desorption energy, the efficiency is similar to the model with a single barrier at 1000 K. The higher H_2 formation rate is due to the H_2 formation by the Eley-Rideal mechanism, whose rate can be as high as the Langmuir-Hinshelwood rate (Le Bourlot et al. 2012). H_2 formation through single hydrogenated PAHs and cation PAHs is less efficient at all temperatures than on silicate grains because the rate is basically an Eley-Rideal mechanism rate. The models assume that only atomic H and D can chemisorb. In more realistic models where the chemisorption sites can be occupied by other species (for example -OH), the efficiency of H_2 formation on silicate grains may decrease and the fraction of H_2 formed via hydrogenated PAHs increases. The H_2 formation rate by H-atom abstraction of hydrogenated PAHs will increase if we adopt a larger abstraction cross-section (see Appendix C). Studies have suggested that cross-sections more than ten times higher than our value may be possible (Zecho et al. 2002b). The additional path to form H_2 through the hydrogenated PAHs is required to explain observed H_2 formation rates that are higher than the theoretical limit set by the H atom impinging rate on grain surfaces. In this study, we have not included H_2 formation via photodissociation of Hydrogenated Amorphous Carbon nano-grains (HACs). Jones & Habart (2015) examined this route and concluded that this mechanism could be efficient for warm grains ($T = 50$–100 K) in moderately UV illuminated regions (with a Draine field $I_{\rm UV} = 1$–100). Duley & Williams (1993) have described a model of H_2 formation on carbonaceous grains at temperartures found in protoplanetary disks. The H_2 formation on HACs will be explored in future studies.

In Fig. 4, we compare the abundances of the standard model with models without chemisorbed species, the analytical Cazaux model and the Jura model (Jura 1974, 1975a,b). As expected the H_2 formation rates in the full surface chemistry and in the analytical model are quasi-identical. The HD formation rate in the Cazaux model is lower than in the other models.

On the right panel of Fig. 2, the effects of different gas and dust temperatures are shown for dust grain temperatures between 10 and 60 K for models that include the Langmuir-Hinshelwood and Eley-Rideal H_2 formation mechanism. The ER H_2 formation is efficient for warm gas and dust, consistent with Le Bourlot et al. (2012). However, the efficiency drops for dust grains above 100 K when the desorption of physisorbed H-atoms start to overtake the transfer of the atom to a chemisorption site compared to

the H_2 formation by the encounter between a physisorbed and a chemisorbed atom. The H_2 formation rate increases with grain surface temperature as expected, although just by a factor two. This enhancement compared to the standard value may be insufficient to explain observations of abundant hot H_2 gas (Habart et al. 2004).

6. Conclusions and perspectives

We have implemented a detailed H_2 and HD formation model in the PRODIMO code. The model extends the rate-equation treatment of surface reactions to chemisorbed species assuming diffusion-reaction competition surface rates. We modeled the Langmuir-Hinshelwood and Eley-Rideal mechanisms for physisorbed and chemisorbed H and D atoms. We introduced the concept of chemisorption sites as a pseudo-species, which facilitates the computation of chemisorbed species. We also accounted for the formation of H_2 and HD on hydrogenated PAH and PAH cations. We implemented a charge exchange chemistry between the PAHs and the other gas-phase species.

The Langmuir-Hinshelwood processes (between two physisorbed H-atoms, between a physisorbed and a chemisorbed atom, and between two chemisorbed atoms) are the main H_2 formation route at all dust temperatures. H_2 also forms efficiently by the Eley-Rideal mechanism between 50 and 100 K. The contribution of singly and multiply-hydrogenated PAHs and PAH ions to the H_2 formation is limited when a small cross-section for hydrogen abstraction is adopted. The value of the cross-section varies by orders of magnitude from study to study. More experimental and theoretical works are warranted before a more definitive conclusion on the importance of H_2 formation through hydrogenated PAHs can be drawn.

HD formation proceeds both on the grain surfaces and in the gas-phase. For all dust temperatures below the chemisorption desorption temperature in the case of low photodesorption, the surface-mediated chemisorption processes dominate over the desorption of physisorbed H-atoms.

Our implementation of a warm surface chemistry can be used to model H_2 and HD formation in photodissociation regions, protoplanetary disks, and other astrophysical environments where the dust temperature is above 20 K. Future studies will include the formation of H_2 on carbonaceous grain surfaces.

References

Abel, T., Bryan, G. L., & Norman, M. L. 2002, Science, 295, 93
Abouelaziz, H., Gomet, J. C., Pasquerault, D., Rowe, B. R., & Mitchell, J. B. A. 1993, J. Chem. Phys., 99, 237
Aikawa, Y., Miyama, S. M., Nakano, T., & Umebayashi, T. 1996, ApJ, 467, 684
Al-Halabi, A., & van Dishoeck E. F. 2007, MNRAS, 382, 1648
Allamandola, L. J., Tielens, A. G. G. M., & Barker, J. R. 1989, ApJS, 71, 733
Allouche, A., Jelea, A., Marinelli, F., & Ferro, Y. 2006, Phys. Scr., 2006, 91
Andrews, H., Candian, A., & Tielens, A. G. G. M. 2016, A&A, 595, A23
Aréou, E., Cartry, G., Layet, J.-M., & Angot, T. 2011, J. Chem. Phys., 134, 014701
Aresu, G., Kamp, I., Meijerink, R., et al. 2011, A&A, 526, A163
Aresu, G., Meijerink, R., Kamp, I., et al. 2012, A&A, 547, A69
Aronowitz, S., & Chang, S. 1980, ApJ, 242, 149
Ásgeirsson, V., Jónsson, H., & Wikfeldt, K. T. 2017, J. Phys. Chem. C, 121, 1648
Bachellerie, D., Sizun, M., Teillet-Billy, D., Rougeau, N., & Sidis, V. 2007, Chem. Phys. Lett., 448, 223
Bakes, E. L. O., & Tielens, A. G. G. M. 1994, ApJ, 427, 822
Barlow, M. J., & Silk, J. 1976, ApJ, 207, 131
Bauschlicher, Jr. C. W. 1998, ApJ, 509, L125

Bauschlicher, C. W., & Ricca, A. 2014, Theor. Chem. Acc., 133, 1454
Bell, R. P. 1980, The Tunnel Effect in Chemistry (New York: Springer US)
Bergin, E. A., Cleeves, L. I., Gorti, U., et al. 2013, Nature, 493, 644
Biennier, L., Alsayed-Ali, M., Foutel-Richard, A., et al. 2006, Faraday Discuss., 133, 289
Bonfanti, M., & Martinazzo, R. 2016, Int. J. Quantum Chem., 116, 1575
Bonfanti, M., Jackson, B., Hughes, K., Burghardt, I., & Martinazzo, R. 2015, J. Chem. Phys., 143, 124703
Boogert, A. C. A., Gerakines, P. A., & Whittet, D. C. B. 2015, ARA&A, 53, 541
Borodin, V. A., Vehviläinen, T. T., Ganchenkova, M. G., & Nieminen, R. M. 2011, Phys. Rev. B, 84, 075486
Boschman, L., Cazaux, S., Spaans, M., Hoekstra, R., & Schlathölter, T. 2015, A&A, 579, A72
Bron, E., Le Bourlot, J., & Le Petit F. 2014, A&A, 569, A100
Brown, R. D., & Rice, E. H. N. 1986, MNRAS, 223, 429
Canosa, A., Parent, D. C., Pasquerault, D., et al. 1994, Chem. Phys. Lett., 228, 26
Casolo, S., Martinazzo, R., Bonfanti, M., & Tantardini, G. F. 2009, J. Phys. Chem. A, 113, 14545
Castellanos, P., Candian, A., Zhen, J., Linnartz, H., & Tielens, A. G. G. M. 2018a, A&A, 616, A166
Castellanos, P., Candian, A., Andrews, H., & Tielens, A. G. G. M. 2018b, A&A, 616, A167
Cazaux, S., & Spaans, M. 2009, A&A, 496, 365
Cazaux, S., & Tielens, A. G. G. M. 2002, ApJ, 575, L29
Cazaux, S., & Tielens, A. G. G. M. 2004, ApJ, 604, 222
Cazaux, S., & Tielens, A. G. G. M. 2010, ApJ, 715, 698
Cazaux, S., Morisset, S., Spaans, M., & Allouche, A. 2011, A&A, 535, A27
Cazaux, S., Boschman, L., Rougeau, N., et al. 2016, Sci. Rep., 6, 19835
Chaabouni, H., Bergeron, H., Baouche, S., et al. 2012, A&A, 538, A128
Chang, Q., Cuppen, H. M., & Herbst, E. 2006, A&A, 458, 497
Chung, D. H. 1971, Geophys. J., 25, 511
Congiu, E., Minissale, M., Baouche, S., et al. 2014, Faraday Discuss., 168, 151
Cuppen, H. M., & Hornekær, L. 2008, J. Chem. Phys., 128, 174707
Cuppen, H. M., Kristensen, L. E., & Gavardi, E. 2010, MNRAS, 406, L11
Dartois, E., & D'Hendecourt, L. 1997, A&A, 323, 534
Demarais, N. J., Yang, Z., Snow, T. P., & Bierbaum, V. M. 2014, ApJ, 784, 25
Dent, W. R. F., Thi, W. F., Kamp, I., et al. 2013, PASP, 125, 477
Diño, W. A., Miura, Y., Nakanishi, H., et al. 2004, Solid State Commun., 132, 713
Downing, C. A., Ahmady, B., Catlow, C. R. A., & de Leeuw N. H. 2013, Phil. Trans. R. Soc. London A Math. Phys. Eng. Sci., 371, 20110592
Draine, B. T., & Li, A. 2001, ApJ, 551, 807
Duley, W. W. 1996, MNRAS, 279, 591
Duley, W. W., & Williams, D. A. 1993, MNRAS, 260, 37
Dumont, F., Picaud, F., Ramseyer, C., et al. 2008, Phys. Rev. B, 77, 233401
Dupuy, J. L., Lewis, S. P., & Stancil, P. C. 2016, ApJ, 831, 54
Dutrey, A., Semenov, D., Chapillon, E., et al. 2014, Protostars and Planets VI (Tucson: University of Arizona Press), 317
Farebrother, A. J., Meijer, A. J. H. M., Clary, D. C., & Fisher, A. J. 2000, Chem. Phys. Lett., 319, 303
Ferro, Y., Marinelli, F., & Allouche, A. 2003, Chem. Phys. Lett., 368, 609
Ferullo, R. M., Castellani, N. J., & Belelli, P. G. 2016, Chem. Phys. Lett., 648, 25
Flower, D. R., & Harris, G. J. 2007, MNRAS, 377, 705
Flower, D. R., & Pineau des Forêts, G. 2003, MNRAS, 343, 390
Flower, D. R., Pineau-Des-Forets, G., & Hartquist, T. W. 1986, MNRAS, 218, 729
Flubacher, P., Leadbetter, A. J., & Morrison, J. A. 1960, J. Chem. Phys., 33, 1751
Forrey, R. C. 2013a, Phys. Rev. A, 88, 052709
Forrey, R. C. 2013b, ApJ, 773, L25
Fournier, J. A., Shuman, N. S., Melko, J. J., Ard, S. G., & Viggiano, A. A. 2013, J. Chem. Phys., 138, 154201
Galli, D., & Palla, F. 1998, A&A, 335, 403
Garcia-Gil, S., Teillet-Billy, D., Rougeau, N., & Sidis, V. 2013, J Phys. Chem. C, 117, 12612
Garrett, B. C., & Truhlar, D. G. 1980, J. Chem. Phys., 72, 3460
Garrod, R. T., & Herbst, E. 2006, A&A, 457, 927
Garrod, R. T., & Pauly, T. 2011, ApJ, 735, 15
Gavilan, L., Lemaire, J. L., & Vidali, G. 2012, MNRAS, 424, 2961
Glover, S. C. O. 2003, ApJ, 584, 331
González-Lezana, T., Honvault, P., & Scribano, Y. 2013, J. Chem. Phys., 139, 054301
Gould, R. J., & Salpeter, E. E. 1963, ApJ, 138, 393
Goumans, T. P. M., Richard, C., Catlow, A., & Brown, W. A. 2009, MNRAS, 393, 1403
Gry, C., Boulanger, F., Nehmé, C., et al. 2002, A&A, 391, 675

Habart, E., Boulanger, F., Verstraete, L., Walmsley, C. M., & Pineau des Forêts, G. 2004, A&A, 414, 531
Hama, T., & Watanabe, N. 2013, Chem. Rev., 113, 8783
Hama, T., Kuwahata, K., Watanabe, N., et al. 2012, ApJ, 757, 185
Haruyama, J., & Watanabe, K. 2011, J. Surf. Sci. Nanotechnol., 9, 1
Hasegawa, T. I., & Herbst, E. 1993, MNRAS, 261, 83
Hasegawa, T. I., Herbst, E., & Leung, C. M. 1992, ApJS, 82, 167
He, J., Frank, P., & Vidali, G. 2011, Phys. Chem. Chem. Phys., 13, 15803
Hickman, A. P. 1979, J. Chem. Phys., 70, 4872
Hincelin, U., Chang, Q., & Herbst, E. 2015, A&A, 574, A24
Hirama, M., Tokosumi, T., Ishida, T., & ichi Aihara J. 2004, Chem. Phys., 305, 307
Hollenbach, D., & McKee, C. F. 1979, ApJS, 41, 555
Hollenbach, D., & Salpeter, E. E. 1970, J. Chem. Phys., 53, 79
Hollenbach, D. J., & Tielens, A. G. G. M. 1999, Rev. Mod. Phys., 71, 173
Hollenbach, D. J., Werner, M. W., & Salpeter, E. E. 1971, ApJ, 163, 165
Honvault, P., & Scribano, Y. 2013, J. Phys. Chem. A, 117, 9778
Hornekær, L., Baurichter, A., Petrunin, V. V., Field, D., & Luntz, A. C. 2003, Science, 302, 1943
Iqbal, W., Acharyya, K., & Herbst, E. 2012, ApJ, 751, 58
Iqbal, W., Acharyya, K., & Herbst, E. 2014, ApJ, 784, 139
Irikura, K. K. 2007, J. Phys. Chem. Ref. Data, 36, 389
Ivanovskaya, V. V., Zobelli, A., Teillet-Billy, D., et al. 2010, Eur. Phys. J. B, 76, 481
Ivlev, A. V., Röcker, T. B., Vasyunin, A., & Caselli, P. 2015, ApJ, 805, 59
Jacobs, T. A., Giedt, R. R., & Cohen, N. 1967, J. Chem. Phys., 47, 54
Jeloaica, L., & Sidis, V. 1999, Chem. Phys. Lett., 300, 157
Jochims, H. W., Ruhl, E., Baumgartel, H., Tobita, S., & Leach, S. 1994, ApJ, 420, 307
Jochims, H. W., Baumgaertel, H., & Leach, S. 1996, A&A, 314, 1003
Jones, A. P., & Habart, E. 2015, A&A, 581, A92
Jones, A. P., & Williams, D. A. 1985, MNRAS, 217, 413
Jura, M. 1974, ApJ, 191, 375
Jura, M. 1975a, ApJ, 197, 581
Jura, M. 1975b, ApJ, 197, 575
Kamp, I., Tilling, I., Woitke, P., Thi, W.-F., & Hogerheijde, M. 2010, A&A, 510, A18
Kamp, I., Thi, W.-F., Woitke, P., et al. 2017, A&A, 607, A41
Karlicky, F., Lepetit, B., & Lemoine, D. 2014, J. Chem. Phys., 140, 124702
Katz, N., Furman, I., Biham, O., Pirronello, V., & Vidali, G. 1999, ApJ, 522, 305
Kerkeni, B., & Bromley, S. T. 2013, MNRAS, 435, 1486
Kerkeni, B., Bacchus-Montabonel, M.-C., & Bromley, S. T. 2017, Mol. Astrophys., 7, 1
Klærke, B., Toker, Y., Rahbek, D. B., Hornekær, L., & Andersen, L. H. 2013, A&A, 549, A84
Klose, S. 1992, A&A, 260, 321
Kuwahata, K., Hama, T., Kouchi, A., & Watanabe, N. 2015, Phys. Rev. Lett., 115, 133201
Lara, M., Jambrina, P. G., Aoiz, F. J., & Launay, J.-M. 2015, J. Chem. Phys., 143, 204305
Launay, J. M., Le Dourneuf, M., & Zeippen, C. J. 1991, A&A, 252, 842
Le Bourlot, J., Le Petit, F., Pinto, C., Roueff, E., & Roy, F. 2012, A&A, 541, A76
Le Petit, F., Roueff, E., & Le Bourlot J. 2002, A&A, 390, 369
Le Petit, F., Barzel, B., Biham, O., Roueff, E., & Le Bourlot J. 2009, A&A, 505, 1153
Leitch-Devlin, M. A., & Williams, D. A. 1984, MNRAS, 210, 577
Li, A., & Draine, B. T. 2001, ApJ, 554, 778
Limbach, H.-H., Miguel Lopez, J., & Kohen, A. 2006, Phil. Trans. R. Soc. London B Biol. Sci., 361, 1399
Ling, Y., & Lifshitz, C. 1998, J. Phys. Chem. A, 102, 708
Linsky, J. L., Diplas, A., Wood, B. E., et al. 1995, ApJ, 451, 335
Luna, R., Luna-Ferrándiz, R., Millán, C., et al. 2017, ApJ, 842, 51
Ma, J., Michaelides, A., & Alfè, D. 2011, J. Chem. Phys., 134, 134701
Manicò, G., Ragunì, G., Pirronello, V., Roser, J. E., & Vidali, G. 2001, ApJ, 548, L253
Martinazzo, R., & Tantardini, G. F. 2006, J. Chem. Phys., 124, 124703
Martinez, O., Yang, Z., Betts, N. B., Snow, T. P., & Bierbaum, V. M. 2009, ApJ, 705, L172
Masuda, K., Takahashi, J., & Mukai, T. 1998, A&A, 330, 773
Matar, E., Congiu, E., Dulieu, F., Momeni, A., & Lemaire, J. L. 2008, A&A, 492, L17
McClure, M. K., Bergin, E. A., Cleeves, L. I., et al. 2016, ApJ, 831, 167
McElroy, D., Walsh, C., Markwick, A. J., et al. 2013, A&A, 550, A36
Meijerink, R., Aresu, G., Kamp, I., et al. 2012, A&A, 547, A68
Mennella, V., Brucato, J. R., Colangeli, L., & Palumbo, P. 1999, ApJ, 524, L71
Mennella, V., Hornekær, L., Thrower, J., & Accolla, M. 2012, ApJ, 745, L2

Michoulier, E., Ben Amor, N., Rapacioli, M., et al. 2018, Phys. Chem. Chem. Phys., 20, 11941

Miller, T. M. 1980, J. Chem. Phys., 72, 4659

Miotello, A., van Dishoeck, E. F., Kama, M., & Bruderer, S. 2016, A&A, 594, A85

Mitchell, D. N., & Le Roy D. J. 1973, J. Chem. Phys., 58, 3449

Montillaud, J., Joblin, C., & Toublanc, D. 2013, A&A, 552, A15

Morisset, S., & Allouche, A. 2008, J. Chem. Phys., 129, 024509

Moseley, J., Aberth, W., & Peterson, J. R. 1970, Phys. Rev. Lett., 24, 435

Moustefaoui, T., Rebrion-Rowe, C., Le Garrec, J.-L., Rowe, B. R., & Mitchell, J. B. A. 1998, Faraday Discuss., 109, 71

Navarro-Ruiz, J., Sodupe, M., Ugliengo, P., & Rimola, A. 2014, Phys. Chem. Chem. Phys., 16, 17447

Navarro-Ruiz, J., Martínez-González, J. A., Sodupe, M., Ugliengo, P., & Rimola, A. 2015, MNRAS, 453, 914

Novotny, O., Sivaraman, B., Rebrion-Rowe, C., et al. 2005, J. Phys. Conf. Ser., 4, 211

Oehrlein, G. S., Schwarz-Selinger, T., Schmid, K., Schlüter, M., & Jacob, W. 2010, J. Appl. Phys., 108, 043307

Ohlinger, L., Forrey, R. C., Lee, T.-G., & Stancil, P. C. 2007, Phys. Rev. A, 76, 042712

Omont, A. 1986, A&A, 164, 159

Oueslati, I., Kerkeni, B., & Bromley, S. T. 2015, Phys. Chem. Chem. Phys., 17, 8951

Palla, F., Salpeter, E. E., & Stahler, S. W. 1983, ApJ, 271, 632

Pasquini, M., Bonfanti, M., & Martinazzo, R. 2016, Phys. Chem. Chem. Phys., 18, 6607

Perets, H. B., Biham, O., Manicó, G., et al. 2005, ApJ, 627, 850

Perets, H. B., Lederhendler, A., Biham, O., et al. 2007, ApJ, 661, L163

Petucci, J., Semone, S., LeBlond, C., Karimi, M., & Vidali, G. 2018, J. Chem. Phys., 149, 014702

Pierson, H. O. 1993, Handbook of Carbon, Graphite Diamond and Fullerenes (Noyes: New Jersey)

Pirronello, V., Liu, C., Shen, L., & Vidali, G. 1997, ApJ, 475, L69

Pirronello, V., Liu, C., Roser, J. E., & Vidali, G. 1999, A&A, 344, 681

Rab, C., Güdel, M., Woitke, P., et al. 2018, A&A, 609, A91

Rasmussen, J. A. 2013, J. Phys. Chem. A, 117, 4279

Rauls, E., & Hornekær, L. 2008, ApJ, 679, 531

Reboussin, L., Wakelam, V., Guilloteau, S., & Hersant, F. 2014, MNRAS, 440, 3557

Reitsma, G., Boschman, L., Deuzeman, M. J., et al. 2014, Phys. Rev. Lett., 113, 053002

Roser, J. E., Manicò, G., Pirronello, V., & Vidali, G. 2002, ApJ, 581, 276

Roueff, E., Herbst, E., Lis, D. C., & Phillips, T. G. 2007, ApJ, 661, L159

Ruaud, M., Wakelam, V., & Hersant, F. 2016, MNRAS, 459, 3756

Rutigliano, M., Cacciatore, M., & Billing, G. D. 2001, Chem. Phys. Lett., 340, 13

Schwenke, D. W. 1988, J. Chem. Phys., 89, 2076

Schwenke, D. W. 1990, J. Chem. Phys., 92, 7267

Sha, X., Jackson, B., Lemoine, D., & Lepetit, B. 2005, J. Chem. Phys., 122, 014709

Shaw, G., Ferland, G. J., Abel, N. P., Stancil, P. C., & van Hoof, P. A. M. 2005, ApJ, 624, 794

Shull, J. M., & Hollenbach, D. J. 1978, ApJ, 220, 525

Simbotin, I., Ghosal, S., & Côté, R. 2011, Phys. Chem. Chem. Phys., 13, 19148

Skov, A. L., Thrower, J. D., & Hornekær, L. 2014, Faraday Discuss., 168, 223

Smith, D., Church, M. J., & Miller, T. M. 1978, J. Chem. Phys., 68, 1224

Smith, D., Adams, N. G., & Alge, E. 1982, ApJ, 263, 123

Snow, T. P., Le Page, V., Keheyan, Y., & Bierbaum, V. M. 1998, Nature, 391, 259

Song, Z., & Xu, H. 2016, Appl. Surf. Sci., 366, 166

Stancil, P. C., & Dalgarno, A. 1997, ApJ, 490, 76

Stancil, P. C., Lepp, S., & Dalgarno, A. 1998, ApJ, 509, 1

Sun, J. C., Choi, B. H., Poe, R. T., & Tang, K. T. 1980, J. Chem. Phys., 73, 6095

Taquet, V., Ceccarelli, C., & Kahane, C. 2012, A&A, 538, A42

Thi, W. F., van Dishoeck, E. F., Blake, G. A., et al. 2001, ApJ, 561, 1074

Thi, W.-F., Woitke, P., & Kamp, I. 2010, MNRAS, 407, 232

Thi, W.-F., Woitke, P., & Kamp, I. 2011, MNRAS, 412, 711

Thi, W. F., Kamp, I., Woitke, P., et al. 2013, A&A, 551, A49

Thrower, J. D., Jørgensen, B., Friis, E. E., et al. 2012, ApJ, 752, 3

Tielens, A. G. G. M. 2005, The Physics and Chemistry of the Interstellar Medium (Cambridge, UK: Cambridge University Press)

Tielens, A. G. G. M., & Allamandola, L. J. 1987, Astrophys. Space Sci. Lib., 134, 397

Tielens, A. G. G. M., Allamandola, L. J., Barker, J. R., & Cohen, M. 1987, in NATO Advanced Science Institutes (ASI) Series C, eds. A. Leger, L. D'Hendecourt, & N. Boccara (Berlin: Springer), 191, 273

Tobita, S. 1992, Chem. Phys., 161, 501

Trainor, D. W., Ham, D. O., & Kaufman, F. 1973, J. Chem. Phys., 58, 4599

Veeraghattam, V. K., Manrodt, K., Lewis, S. P., & Stancil, P. C. 2014, ApJ, 790, 4

Verstraete, L., Leger, A., D'Hendecourt, L., Defourneau, D., & Dutuit, O. 1990, A&A, 237, 436

Vidali, G. 2013, Chem. Rev., 113, 8762

Vidali, G., Pirronello, V., Li, L., et al. 2007, J. Phys. Chem. A, 111, 12611

Wakelam, V., & Herbst, E. 2008, ApJ, 680, 371

Wakelam, V., Bron, E., Cazaux, S., et al. 2017, Mol. Astrophys., 9, 1

Watanabe, N., Kimura, Y., Kouchi, A., et al. 2010, ApJ, 714, L233

Watson, W. D. 1973, ApJ, 182, L73

Watson, W. D. 1976, Rev. Mod. Phys., 48, 513

Weingartner, J. C., & Draine, B. T. 2001, ApJS, 134, 263

Whitlock, P. A., Muckerman, J. T., & Roberts, R. E. 1974, J. Chem. Phys., 60, 3658

Woitke, P., Kamp, I., & Thi, W.-F. 2009, A&A, 501, 383

Woitke, P., Min, M., Pinte, C., et al. 2016, A&A, 586, A103

Wolf, M., Kiefer, H. V., Langeland, J., et al. 2016, ApJ, 832, 24

Wolfire, M. G., Tielens, A. G. G. M., Hollenbach, D., & Kaufman, M. J. 2008, ApJ, 680, 384

Zecho, T., Guttler, A., Sha, X., Jackson, B., & Kuppers, J. 2002a, J. Chem. Phys., 117, 8486

Zecho, T., Güttler, A., Sha, X., et al. 2002b, Chem. Phys. Lett., 366, 188

Appendix A: Sticking coefficient

Although the sticking coefficient can modify the H_2 (HD) formation rate, it does not affect the efficiency of the surface recombination. We discuss here a simple qualitative model, which can help us understand the behaviour of the sticking coefficient as a function of the parameters such as gas and dust temperature as well as the binding energy.

The Goodman's version of the modified Baule formula gives the transfer of energy between the incident particle and the surface accounting for a surface at temperature T_d (Bonfanti & Martinazzo 2016)

$$\delta\epsilon = 2.4 \frac{\alpha}{(1+\alpha)^2} \left(\epsilon + D - \frac{1}{2}kT_d\right), \tag{A.1}$$

where α is the mass ratio between the incident species of mass m_i to the mass of the surface atom m_{surf}, ϵ is the kinetic energy of the collision at temperature T_g ($\epsilon = (1/2)kT_g$), $\langle (1/2)m_s v_{surf}^2 \rangle = (1/2)kT_d$, where $\langle v_{surf}^2 \rangle = \hbar\omega_{surf}/2m_{surf}$ for an harmonic oscillator of frequency ω_{surf}, E_i^b is the binding energy, the surface is at temperature T_d. $D = 3/4E_i^b$ as suggested by Hollenbach & Salpeter (1970). The original Baule formulation uses a pre-factor of 4 instead of 2.4. When $\epsilon + D - \frac{1}{2}kT_d < 0$, the species returns to the gas-phase with extra energy acquired from the surface. Alternatively, one can use the formula in Hollenbach & Salpeter (1970) modified to account for the dust surface temperature. First we define a characteristic frequency of the repulsive collision

$$\omega_0 = \left[(\epsilon + D - 0.5kT_d)/2m_i b^2\right]^{1/2}, \tag{A.2}$$

where b is the experimental determined slope parameter with a value $b = 0.30$Å from Hollenbach & Salpeter (1970). When $1 \lesssim \omega/\omega_0 \leqslant 1.68$ where ω is the Debye frequency of the solid such that $h\omega/2\pi = k\theta_D$, with θ_D being the Debye temperature in Kelvin,

$$\delta\epsilon = \alpha\left(\epsilon + D - \frac{1}{2}kT_d\right). \tag{A.3}$$

For crystalline water ice, we use $\theta_D = 222.2$ K (Flubacher et al. 1960), which gives $\omega = 2.9 \times 10^{13}$ s^{-1} compared to $\omega_0 = 4 \times 10^{13}$ s^{-1} at 78 K (Hollenbach & Salpeter 1970). The Debye temperature for crystalline olivine is 753 K (Chung 1971). When $\omega/\omega_0 > 1.68$

$$\delta\epsilon = \alpha\left(\epsilon + D - \frac{1}{2}kT_d\right) 2\left[\omega_0^2/(\omega^2 - \omega_0^2)\right]. \tag{A.4}$$

The sticking coefficient is within about 5% of the value found by (Hollenbach & Salpeter 1970)

$$S \approx \frac{\gamma^2 + 0.8\gamma^3}{1 + 2.4\gamma + \gamma^2 + 0.8\gamma^3}, \tag{A.5}$$

where $\gamma \equiv E_i^c/kT_g$, $E_i^c = \Omega\left(D\delta\epsilon\right)^{1/2}$. Ω is a factor that accounts for the type of surface rebonds: $\Omega^2 \simeq 1$ for Lambert's law and $\Omega^2 = 2$ for isotropic scattering above the surface (Hollenbach & Salpeter 1970). We choose $\Omega^2 = 2$, consistent with a rough surface. The sticking coefficient reduces to $S \simeq \gamma^2$ for $\gamma \ll 1$ (inefficient energy transfer) and to $S \simeq 1 - 3/\gamma^2$ for $\gamma \gg 1$ (efficient energy transfer). The sticking coefficient increases with the binding energy. Hollenbach & Salpeter (1970) used a value $\delta\epsilon = 17$ K for H collisions with water ice.

Appendix B: PAH charge exchange chemistry

Table B.1. Circumcoronene electron affinity and ionisation potential.

	E.A. (eV)	I.P. (eV) lit.	I.P. WD2001
$C_{54}H_{18}$	1.3	5.9	6.2
$C_{54}H_{18}^+$	...	8.8	9.4
$C_{54}H_{18}^{2+}$	...	12.9	12.5

Notes. The measured (lit.) and computed (WD2001) values are shown.

A model of PAH ionisation has been presented by Dartois & D'Hendecourt (1997). We use the circumcoronene ($C_{54}H_{18}$) as a typical PAH that is large enough to escape photodissociation in disks around HerbigAe stars. The circumcoronene can be once negatively-charged (PAH$^-$) and three times positively charged by absorbing a UV with energy below 13.6 eV or by charge exchange reactions (PAH$^+$, PAH^{2+}, PAH^{3+}, see Table B.1). The effective radius of a PAH is computed by Weingartner & Draine (2001)

$$a_{PAH} = 10^{-7} \left(\frac{N_C}{468}\right)^{1/3} \text{ cm}, \tag{B.1}$$

where N_C is the number of carbon atoms in the PAH. The radius for the circumcoronene is $a_{PAH}(C_{54}H_{18}) = 4.686 \times 10^{-8}$ cm. The PAH ionisation potential can either be taken from the literature when they are measured or estimated (Weingartner & Draine 2001)

$$IP_{PAH} = W_0 + (Z_{PAH} + 0.5)\frac{e^2}{a_{PAH}} +$$
$$(Z_{PAH} + 2)\frac{e^2}{a_{PAH}}\frac{0.3 \times 10^{-8}}{a_{PAH}} \text{ erg}, \tag{B.2}$$

where W_0 is the work function assumed to be 4.4 eV (7.05×10^{-12} erg), and Z_{PAH} is the charge of the PAH. The ionisation potentials (I.P.) are listed in Table B.1.

B.1. PAH photoionisation and PAH$^-$ photodetachment

Stellar and interstellar ultraviolet (UV) photons with energy below 13.6 eV ionise neutral and ionised PAHs in disk surfaces

$$\text{PAH} + h\nu \rightarrow \text{PAH}^+ + e^-. \tag{B.3}$$

The photoionisation rates at each disk location were computed by integrating the product of the photoionisation cross-sections calculated using the PAH model of Li & Draine (2001) with the internal UV field obtained by solving the continuum dust radiative transfer and a yield computed according to the prescription of Jochims et al. (1996). PAH self-shielding is taken into account. PAH$^-$ can loose its electron by absorbing a stellar or interstellar UV photon (photodetachment)

$$\text{PAH}^- + h\nu \rightarrow \text{PAH} + e^-. \tag{B.4}$$

The rates are computed the same way as for the photoionisation.

Table B.2. PAH cation recombination rate coefficients measured at room temperature (300 K) by Biennier et al. (2006).

Name	Formula	k [cm^3 s^{-1}]	Ref.
Naphtalene	$C_{10}H_8^+$	$0.3(\pm 0.1) \times 10^{-6}$	[a]
Azulene	$C_{10}H_8^+$	$1.1(\pm 0.1) \times 10^{-6}$	"
Acenaphtalene	$C_{12}H_{10}^+$	$0.5(\pm 0.2) \times 10^{-6}$	"
Anthracene	$C_{14}H_{10}^+$	$2.4(\pm 0.8) \times 10^{-6}$	"
Phenanthrene	$C_{14}H_{10}^+$	$1.7(\pm 0.5) \times 10^{-6}$	"
Fluoranthene	$C_{16}H_{10}^+$	$3.0(\pm 0.9) \times 10^{-6}$	"
Pyrene	$C_{16}H_{10}^+$	$4.1(\pm 1.2) \times 10^{-6}$	"
Naphtalene	$C_{10}H_8^+$	$0.3(\pm 0.1) \times 10^{-6}$	[b]
Anthracene	$C_{14}H_{10}^+$	$1.1(\pm 0.5) \times 10^{-6}$	[c]

Notes. Alternative values are also listed in the bottom of the table.

References. [a] Biennier et al. (2006); [b] Abouelaziz et al. (1993); [c] Novotny et al. (2005).

B.1.1. Energetic particles induced photoionisation and photodetachment

H$_2$ collisionally excited to Rydberg states by fast secondary electrons fluoresces in the ultraviolet. These secondary electrons are generated by energetic particles (cosmic ray, X-ray, or radioactive decay) ionizing hydrogen nuclei. The fluorescence photons have enough energy to remove an electron from a PAH

$$\text{PAH} + \text{MUV} \rightarrow \text{PAH}^+ + e^-, \tag{B.5}$$

or detach an electron from a PAH anion

$$\text{PAH}^- + \text{MUV} \rightarrow \text{PAH} + e^-, \tag{B.6}$$

where MUV stands for UV generated by gas interaction with MeV particles. The number of fluorescence photons with energies between 7.1 and 14.6 eV is $f_{Ryd}\zeta n_H$ (Flower & Pineau des Forêts 2003), where f_{Ryd} is the fraction of the secondary electrons that excite the H$_2$, ζ is the rate (s^{-1}) of total hydrogen ionisation (cosmic ray, X-ray, and radioactive decay). We adopted a value of 0.15 for f_{Ryd} (Flower & Pineau des Forêts 2003). The rate coefficient for photoionisation triggered by energetic events is

$$k_{pi,MeV} = 0.15 \zeta n_H g_{PAH} y_{pi} \text{ cm}^{-3} \text{ s}^{-1} \text{ cm}^3 \text{ s}^{-1}, \tag{B.7}$$

where g_{PAH} is the fraction of the photons absorbed by the neutral or positive PAHs compared to the total opacity and y_{pi} is the yield of photodetachment. Likewise, the rate coefficient for photodetachment is

$$k_{pd,CR} = 0.15 \zeta n_H g_{PAH^-} y_{pd} \text{ cm}^{-3} \text{ s}^{-1}, \tag{B.8}$$

where g_{PAH^-} the fraction of the photons absorbed by the negative PAHs and y_{pd} is the yield of photodetachment. The reactions may be important in the UV-shielded environments

B.1.2. Electron recombination

Ionised PAHs can recombine with electrons. The electron recombination rate with singly-ionised PAHs

$$\text{PAH}^+ + e^- \rightarrow \text{PAH} \tag{B.9}$$

Table B.3. Circumcoronene cation electron recombination rate coefficients ($\phi_{PAH} = 0.4$).

Formula	k [cm^3 s^{-1}]
$C_{54}H_{18}^+$	$1.7 \times 10^{-5} \left(\frac{100K}{T}\right)^{1/2}$
$C_{54}H_{18}^{++}$	$1.7 \times 10^{-5} \left(\frac{100K}{T}\right)^{1/2} \left(1 + \frac{36438.8}{T}\right)$
$C_{54}H_{18}^{+++}$	$1.7 \times 10^{-5} \left(\frac{100K}{T}\right)^{1/2} \left(1 + \frac{72877.6}{T}\right)$
HCO$^+$	$3.0 \pm 0.9 \times 10^{-7} \left(\frac{T}{300K}\right)^{-0.74 \pm 0.02}$

Notes. By comparison the recombination rate coefficient for HCO$^+$ is also shown.

are calculated following a classical formalism by assuming that PAH-cations and electrons interact via a Coulomb potential (Bakes & Tielens 1994; Tielens 2005):

$$k_{er} = 4.1 \times 10^{-5} \phi_{PAH} f(a_{PAH}) \left(\frac{N_C}{50}\right)^{1/2} \left(\frac{100\,K}{T_g}\right)^{1/2} \text{ cm}^3 \text{ s}^{-1}, \tag{B.10}$$

where N_C is the number of carbon atoms and ϕ_{PAH} a correction factor for the disk shape: $\phi_{PAH} = \sigma_{disk}/\sigma_{sphere}$ between 0.1 and 0.8 (Verstraete et al. 1990). The recombination is essentially not dissociative for the large PAHs present in disks. An experimental study of the recombination of PAH cations with electron has been performed by Biennier et al. (2006) at room temperature for seven small PAH cations. For multiply-ionised PAHs, the recombination rate is enhanced

$$k'_{er} = k_{er} \times \left(1 + \frac{W_{PAH}}{kT_{elec}}\right), \tag{B.11}$$

where $W_{PAH} = IP_{PAH}(Z_{PAH}) - IP_{PAH}(0)$ is the work function and is equal to the difference in ionisation potential between the charged and neutral PAH. If no experimental results exist, we assumed $T_{elec} = T$. We assumed that the recombination of PAH-H$^+$ cations are dissociative and have the same rates as for PAH cations. For PAH with fewer than 20 carbon atoms, an additional correction factor has to be applied to match the experimental data

$$f(a_{PAH}) = \frac{1 - \exp\left(-12 \times a_{PAH}/l_{e^-}\right)}{1.0 + \exp\left(12 - N_C\right)}, \tag{B.12}$$

where a_{PAH} is the PAH radius in cm and the electron escape lengths $l_{e^-} = 10^{-7}$ cm (Weingartner & Draine 2001). Alternatively, Flower & Pineau des Forêts (2003) adopted a size-independent rate

$$k_{er} = 3.3 \times 10^{-6} \left(\frac{300K}{T}\right)^{1/2} \text{ cm}^3 \text{ s}^{-1}. \tag{B.13}$$

Both rates can be reconciled if we take $\phi_{PAH} \simeq 0.2$. For PAHs with 10 carbon atoms or fewer, the recombinations are dissociative (Abouelaziz et al. 1993; Fournier et al. 2013). The comparison between the adopted rates and the laboratory data for singly-ionised PAH cations is shown in Fig. B.1.

The derived recombination rates assuming $\phi_{PAH} \simeq 0.4$ for circumcoronene are given in Table B.3. The rate coefficients as function of the gas temperature are shown in Fig. B.2.
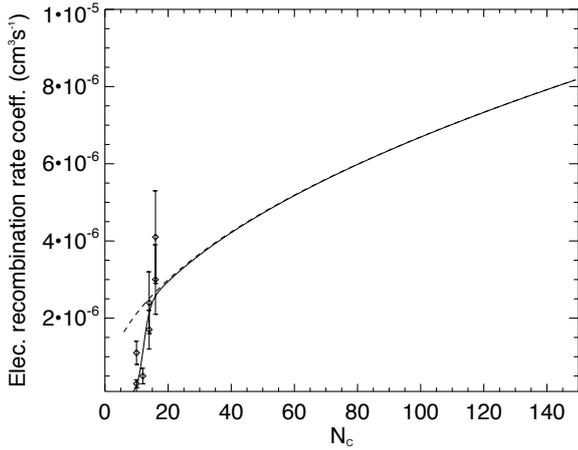
Fig. B.1. PAH$^+$ cation electron recombination rate coefficient as function of the number of carbon atoms using Eq. (B.10) assuming $\phi_{PAH} = 0.2$ and $T = 300$ K (dashed-line). The experimental data from Biennier et al. (2006) are listed in Table B.2. The solid line includes the additional correction $f(a_{PAH})$ for PAHs of radius a_{PAH} applied to the adopted law to match the experimental data.
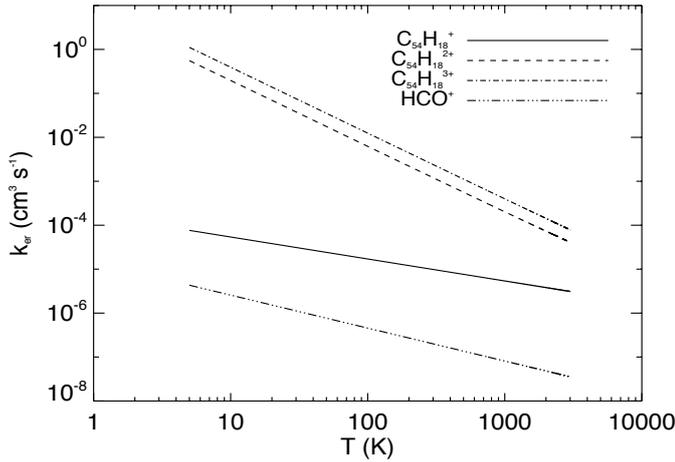
Fig. B.2. Electron recombination rate coefficients for the PAH cations.

Fig. B.3. PAH electron sticking coefficient.

Fig. B.4. PAH rate coefficients. The solid line is the electron attachment rate coefficient. The diamond is the measured PAH attachment rate coefficient for anthracene (Canosa et al. 1994). The dashed- and dashed-dotted lines are the mutual neutralisation rates of C$^+$ at two kinetic temperatures.

B.1.3. Electron attachment

Electrons can attach on neutral PAHs. Experiments have shown that the electron attachment cross section is a strong function of the electron affinity (Tobita 1992), which changes the electron sticking coefficient $S_{PAH}(e^-)$. The electron attachment rate can be written as (Allamandola et al. 1989)

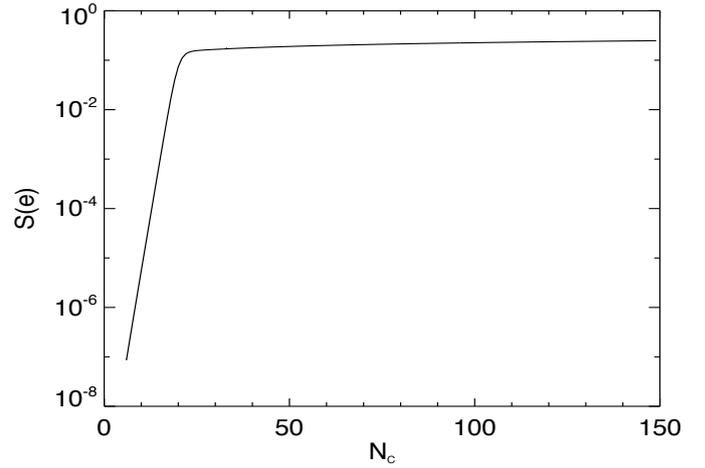$$k_{ea} = S_{PAH}(e^-)k_f \text{ cm}^3 \text{ s}^{-1}, \tag{B.14}$$

where k_f is the electron capture rate. We adopt the sticking coefficient analytical formula from Weingartner & Draine (2001)

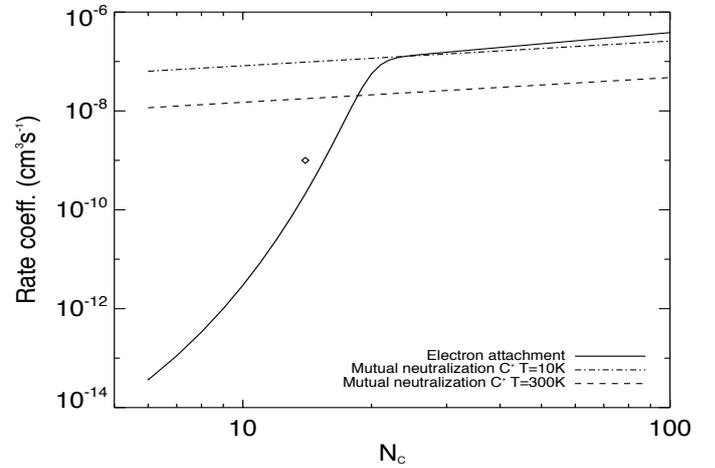$$S_{PAH}(e^-) = \frac{1 - e^{-(a_{PAH}/l_{e^-})}}{1 + e^{(20 - N_C)}}, \tag{B.15}$$

where a_{PAH} is the radius of the PAH in cm and l_{e^-} is the electron escape length equal to 10^{-7} cm (see Fig. B.3). The capture rate follows a Langevin law and thus does not depend on the temperature

$$k_f = 8.5 \times 10^{-7} \phi_{PAH} \sqrt{N_C}. \tag{B.16}$$

Large PAHs ($N_C > 20$) have an electron affinity large enough ($\sim$1 eV) such that the electron sticking coefficient on PAHs $S(e^-)$ is close to unity. The electron attachment rate is approximated by

$$k_{ea} = 8.5 \times 10^{-7} S_{PAH}(e^-) \phi_{PAH} \left(\frac{N_C}{50}\right)^{1/2} \text{ cm}^3 \text{ s}^{-1}. \tag{B.17}$$

This last rate is high compared to the atomic electronic attachment rate coefficients, whose values are 10^{-16}-10^{-14} cm^3 s^{-1}. The electron attachment rate as function of the number of carbons N_C is displayed in Fig. B.4. The formula is consistent with the measured value of 10^{-9} cm^3 $^{-1}$ for anthracene (C$_{14}$H$_{10}$) by Canosa et al. (1994). Other measurements by Moustefaoui et al. (1998) show that the rate is temperature independent and lies between 1 and 3×10^{-9} cm^3 s^{-1} for anthracene, consistent with our choice. For $N_C = 30$, our rate is 10 times smaller than in other studies because they adopt a $N_C^{3/4}$ scaling (Wakelam & Herbst 2008; Omont 1986).

B.1.4. PAH mutual neutralisation reactions

The mutual neutralisation reaction between any atomic cation X^+ and PAH

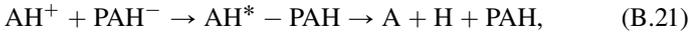$$X^+ + PAH^- \rightarrow X^* - PAH \rightarrow X + PAH^*, \quad (B.18)$$
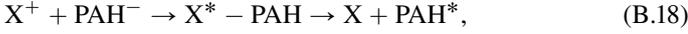
where X^* and PAH^* are excited intermediate species, proceeds at the rate

$$k_{mn} = 2.9 \times 10^{-7} \phi_{PAH} \left(\frac{12 \text{ amu}}{m_X} \right)^{1/2}$$
$$\times \left(\frac{100 \text{ K}}{T} \right)^{1/2} \left(\frac{N_C}{50} \right)^{1/2} \text{ cm}^3 \text{ s}^{-1}, \quad (B.19)$$
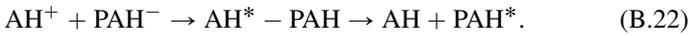
where m_X is the mass of species X and amu is the atomic mass unit. An alternative parametrisation has been proposed to match the experimental mutual neutralisation of simple and clustered positive and negative ions (Hickman 1979)

$$k_{mn} = 5.33 \times 10^{-7} (T/300)^{-0.5}$$
$$\times \mu^{-0.5} (E.A.)^{-0.4} \text{ cm}^3 \text{ s}^{-1}, \quad (B.20)$$

where the reduced mass μ of the ion pair is in atomic mass units and the electron affinity $E.A.$ (electron detachment energy of the negative ion) is in eV. The latter formula has been shown to be quite successful in fitting laboratory data (Miller 1980; Smith, Church, & Miller 1978). For HCO^+, $\mu \simeq 29$ amu. The electron affinity is ~ 1 eV for large PAHs. The temperature-dependence is the same for the two parameterisations. For a molecular cation AH^+ the mutual neutralisation can be dissociative

$$AH^+ + PAH^- \rightarrow AH^* - PAH \rightarrow A + H + PAH, \quad (B.21)$$

or not

$$AH^+ + PAH^- \rightarrow AH^* - PAH \rightarrow AH + PAH^*. \quad (B.22)$$

The branching ratio between the two modes is unknown. In the gas phase, electronic recombinations are dissociative because the ionisation potentials are higher than the A–H bond energy. In the case of the recombination with negatively-charged PAHs the excess energy can be transferred to the PAHs, which have enough vibrational modes to decay rapidly. In this work, both branches are assumed to have the same probability (0.5). All atomic and molecular ions react with PAH^- and we adopt the first parametrisation. The rate at 10 and 300 K for a carbon ions and with $\phi_{PAH} = 0.2$ is shown in Fig. B.4.

B.1.5. PAH collisional detachment reactions

Neutral species can detach the electron from negatively-charged PAHs

$$PAH^- + X \rightarrow PAH + X + e^-. \quad (B.23)$$

The rate follows the prescription of Flower & Pineau des Forêts (2003)

$$k_{nd} = 1.5 \times 10^{-8} \phi_{PAH} \left(\frac{1 \text{ amu}}{m_X} \right)^{1/2} \left(\frac{N_C}{50} \right)^{1/2}$$
$$\times e^{-5500/T} \text{ cm}^3 \text{ s}^{-1}, \quad (B.24)$$

with $\phi_{PAH} = 0.2$. The activation barrier is $E_a/k = 5500$ K. Therefore, PAHs will be more neutralised by this process in hot disk mid-planes.

B.1.6. PAH charge exchange reactions

Neutral and positively-charged PAHs can undergo charge exchanges with ions

$$X^+ + PAH^{n+} \rightarrow X + PAH^{(n+1)+}, \quad (B.25)$$
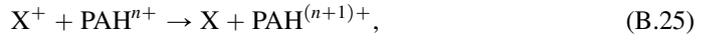
where $n \geqslant 0$. The criterium for the reaction to proceed is that the reaction is energetically allowed, when the ionisation potential (I.P.) of species X is higher than that of PAH^{n+}. Flower & Pineau des Forêts (2003) adopted a reaction probability of 0.1 per collision for reactions with $n = 0$. We adopt the rate coefficients from Tielens (2005) for $n = 0$

$$k_{ce,0} = 2.9 \times 10^{-8} \phi_{PAH} \left(\frac{1 \text{ amu}}{m_X} \right)^{1/2}$$
$$\times \left(\frac{100 \text{ K}}{T} \right)^{1/2} \left(\frac{N_C}{50} \right)^{1/2} \text{ cm}^3 \text{ s}^{-1} \quad (B.26)$$

and

$$k_{ce,n} = k_{ce,0} \times \max \left(0, 1 - \frac{ne^2}{a_{PAH}kT} \right) \text{ cm}^3 \text{ s}^{-1}, \quad (B.27)$$

for positively-charged PAHs ($n > 0$) where the effect of the repulsive potential between the two positively-charged species is taken into account. Assuming that the PAH is a circumcoronene, the minimum temperature required to overcome the repulsion is

$$T_{min} > \frac{e^2}{a_{PAH}k} = 16\,710 \left(\frac{N_C}{468} \right)^{-1/3} \text{ K}. \quad (B.28)$$

For circumcoronene, there is no realistic gas temperature for which the rate $k_{ce,n>0}$ is not zero. Alternatively one can use

$$k_{ce,n} = k_{ce,0} \times \max \left(0, 1 - \frac{W_{PAH}}{kT} \right) \text{ cm}^3 \text{ s}^{-1}. \quad (B.29)$$

For singly positively-charge PAH circumcoronene $W_{PAH} = 2.9$ eV or 33 652.9 K. Both formulations show that only large singly-charged PAHs can exchange charge with cations at high gas temperatures. In protoplanetary disk conditions, those reactions do not occur.

Tielens (2005) also considers a double electron transfer from He^+ to neutral PAHs because of the high value of the helium ioniation potential

$$He^+ + PAH \rightarrow He + PAH^{2+} + e^-, \quad (B.30)$$
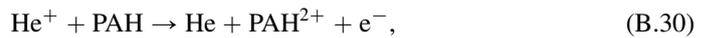
with the rate

$$k_{di} = 1.1 \times 10^{-8} \phi_{PAH} \left(\frac{N_C}{50} \right)^{1/2} \text{ cm}^3 \text{ s}^{-1}. \quad (B.31)$$

Inversely, positively-charged PAHs can gain an electron from ions

$$X + PAH^{n+} \rightarrow X^+ + PAH^{(n-1)+}. \quad (B.32)$$
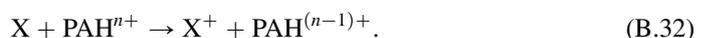
Among the major atomic and molecular species, only sodium (Na) has an I.P. that is lower than that of the adopted PAH.

B.2. PAH adsorption on grain surfaces

In addition to the hydrogenation, neutral PAHs can be ionised or condense (physisorption) onto grain surfaces with an adsorption energy that scales with the number of hydrogen and carbon atoms (Kamp et al. 2017):

$$E_{\mathrm{PAH,des}}/k = 482 \times (N_C - N_H) + 946 \times N_H \text{ K},\qquad(\text{B.33})$$

where E_{CC} (= 482 K) is the fitted desorption energy per graphene-like carbon ($N_{CC} = N_C - N_H$), and E_{CH} (= 946 K) is the fitted energy per benzene-like carbon and its adjoining H-atom ($N_{CH} = N_H$). Graphenes are completely de-hydrogenated PAHs. Graphene-like carbons are C-atoms with three covalent bonds with carbons, whereas benzene-like carbon have two covalent bonds with carbons and one bond with a hydrogen atom. For circumcoronene ($N_{CC} = 36$ and $N_{CH} = 18$), the estimated desorption energy is 34 380 K. The highest possible value is set by the heat of vaporisation for graphite at $H_f/k = 86\,240$ K (Pierson 1993). Michoulier et al. (2018) have calculated the binding energy of PAHs on water ice. For coronene, they found binding energies between 20 330 and 28 140 K, compared to a value of 17 136 K derived using our formula. For simplification, we chose to use the same adsorption energy independent of the type of surface.

Appendix C: Multi-hydrogenated PAHs

We ran three series of molecular cloud models with physisorption only and H_2 formation on multi-hydrogenated PAHs (up to PAH-H_{18}) and without deuterium chemistry. One series of models was run with a standard hydrogen abstraction cross-section of $\sigma = 0.06$ Å^2 and the other series with a tenfold cross-section ($\sigma = 0.6$ Å^2) and hundredfold cross-section ($\sigma = 6$ Å^2). Figure C.1 shows that unless a large cross-section is assumed, the H_2 formation through hydrogenated PAHs is not as efficient as via chemisorbed H atoms at temperatures higher than 100 K. The H_2 formation rate with large cross-sections are higher than on silicate grain surfaces for temperatures higher than 200 K. The high H_2 formation rate below 20 K is due to the formation from physisorbed H-atoms on (icy) silicate grains.

The asymptotic theoretical maximum H_2 formation rate can be estimated by

$$R_{\mathrm{PAH-H_x,max}} = \sigma(kT_g/(2\pi m_H))^{1/2}(n_{\mathrm{PAH}}/n_H)\bar{x},\qquad(\text{C.1})$$

where $\chi_{\mathrm{PAH}} = n_{\mathrm{PAH}}/n_H$ is the PAH abundance and $\bar{x}$ the average hydrogenation state of the PAHs. Introducing the numerical values, the maximum rate becomes

$$R_{\mathrm{PAH-H_x,max}} \simeq 10^{-16} f_{\mathrm{PAH}} \left(\frac{\sigma}{10\,\text{Å}^2}\right)$$
$$\times \left(\frac{T_g}{100\,\text{K}}\right)^{1/2}\left(\frac{\bar{x}}{10}\right) \text{ s}^{-1}.\qquad(\text{C.2})$$

We show the theoretical maximum H_2 formation rate using this formula with $f_{\mathrm{PAH}} = 1$, $x = 18$, and $\sigma = 6$ Å^2 in Fig. C.1.
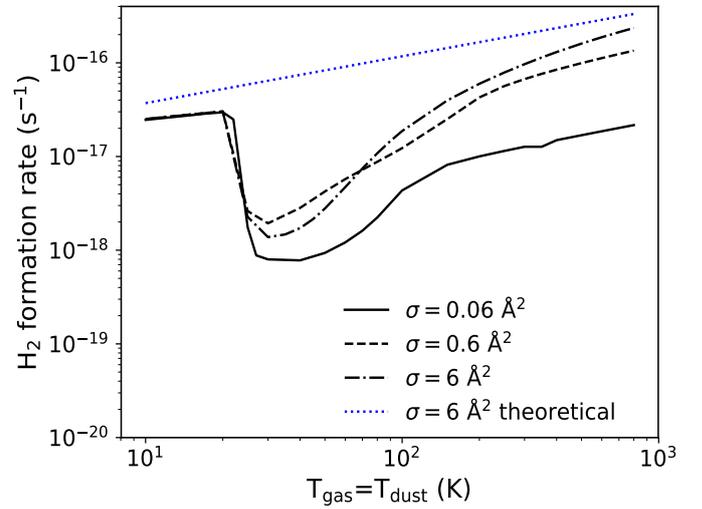
Fig. C.1. H_2 formation rate with adsorbed H on grains and multi-hydrogenated PAHs (up to PAH-H_{18}). The two series show the effect of assuming the abstraction cross-section from Mennella et al. (2012) and when assuming a tenfold and a hundredfold cross-section.

Appendix D: Chemical network

The species modeled in this study are shown in Table D.1.

Table D.1. Gas and solid species in the network.

12 elements	H, He, C, N, O, Ne, Na, Mg, Si, S, Ar, Fe	
(H)	H, H^+, H^-, $\mathbf{H_2}$, H_2^+, H_3^+, H_2^{exc}	7
(He)	He, He^+,	2
(C–H)	C, C^+, C^{++}, CH, CH^+, $\mathbf{CH_2}$, CH_2^+, CH_3, CH_3^+, $\mathbf{CH_4}$, CH_4^+, CH_5^+,	12
(C–N)	CN, CN^+, $\mathbf{HCN}$, HCN^+, $HCNH^+$	5
(C–O)	$\mathbf{CO}$, CO^+, HCO, HCO^+, $\mathbf{CO_2}$, CO_2^+, HCO_2^+,	7
(N–H)	N, N^+, N^{++}, NH, NH^+, NH_2, NH_2^+, $\mathbf{NH_3}$, NH_3^+, NH_4^+	9
(N–N)	$\mathbf{N_2}$, N_2^+, HN_2^+,	3
(N–O)	NO, NO^+,	2
(O–H)	O, O^+, O^{++}, OH, OH^+, $\mathbf{H_2O}$, H_2O^+, H_3O^+,	8
(O–O)	$\mathbf{O_2}$, O_2^+,	2
(O–S)	SO, SO^+, $\mathbf{SO_2}$, SO_2^+, HSO_2^+	5
(S–H)	S, S^+, S^{++},	3
(Si–H)	Si, Si^+, Si^{++}, SiH, SiH^+, SiH_2^+,	6
(Si–O)	$\mathbf{SiO}$, SiO^+, $SiOH^+$,	3
(Na)	Na, Na^+, Na^{++},	3
(Mg)	Mg, Mg^+, Mg^{++},	3
(Fe)	Fe, Fe^+, Fe^{++},	3
(Ne)	Ne, Ne^+, Ne^{++},	3
(Ar)	Ar, Ar^+, Ar^{++},	3
ice	CO#, H_2O#, CO_2#, CH_4#, NH_3#, SiO#, SO_2#, O_2#, HCN#, N_2#,	10
Additional elements	PAH, *	2
Additional species	H#, H_2#, *H#, D, D+, D-, HD, D#, HD#, *D#, $H2D^+$, HDO, HDO#, PAH, PAH^-, PAH^+, PAH#, PAH-H, $PAH-H^+$, PAH-H#, PAHD, PAH-D#, $PAH-D^+$	23
Species	Total	123

Notes. Closed-shell molecules are indicated in bold font, ices are indicated by a trailing #, and chemisorbed species are lead by a * sign. CH_2 is a reactive closed-shell species.

Table D.2. Main grain reactions involved in the formation and destruction of H_2 and HD.

								Reaction	Comment
1			H	$\rightarrow$	H#				Physisorption, barrierless
2			D	$\rightarrow$	D#				–
3	H	+	*	$\rightarrow$	*H#				$E_H^{gc} = E_*^{act} = (400)\ 900\text{--}15\,900$ K
4	H#	+	*	$\rightarrow$	*H#				$E_{H\#}^{pc} = E_*^{act}$
5	D	+	*	$\rightarrow$	*D#				$E_D^{gc} = E_*^{act} + \Delta E^{H-D}$
6	D#	+	*	$\rightarrow$	*D#				$E_{D\#}^{pc} = E_*^{act} + \Delta E^{H-D}$
7			H#	$\rightarrow$	H				$E_{H\#}^{b} = 600$ K
8			D#	$\rightarrow$	D				$E_{D\#}^{b} = E_{H\#}^{b} + \Delta E^{H-D}$
9	H#	+	$h\nu$	$\rightarrow$	H				Photodesorption
10	D#	+	$h\nu$	$\rightarrow$	D				–
11	H#	+	CR	$\rightarrow$	H				
12	D#	+	CR	$\rightarrow$	D				
13			*H#	$\rightarrow$	H	+	*		$E_{*H\#}^{b} = 10,000\text{--}25\,000$ K
14			*D#	$\rightarrow$	D	+	*		$E_{*D\#}^{b} = E_{*H\#}^{b} + \Delta E^{H-D}$
15	*H#	+	$h\nu$	$\rightarrow$	H	+	*		
16	*D#	+	$h\nu$	$\rightarrow$	D	+	*		
17	*H#	+	CR	$\rightarrow$	H	+	*		Via CR induced UV
18	*D#	+	CR	$\rightarrow$	D	+	*		–
19	H	+	H#	$\rightarrow$	H_2				Eley–Rideal (ER) mechanism, barrierless
20	D	+	H#	$\rightarrow$	HD				–
21	H	+	D#	$\rightarrow$	HD				–
22	H#	+	H#	$\rightarrow$	H_2				$E_{H\#,H\#}^{act} = 0\text{--}250$ K (Navarro-Ruiz et al. 2014)
23	H#	+	D#	$\rightarrow$	HD				$E_{H\#,D\#}^{act} = E_{H\#,H\#}^{act} + \Delta E^{H-D} = 0\text{--}308$ K
24	H	+	*H#	$\rightarrow$	H_2	+	*		ER mechanism, barrierless
25	H	+	*D#	$\rightarrow$	HD	+	*		–
26	D	+	*H#	$\rightarrow$	HD	+	*		–
27	H#	+	*H#	$\rightarrow$	H_2	+	*		$E_{*H\#,H\#}^{act} = E_*^{act}$
28	H#	+	*D#	$\rightarrow$	HD	+	*		$E_{*H\#,H\#}^{act} = E_*^{act} + \Delta E^{H-D}$
29	D#	+	*H#	$\rightarrow$	HD	+	*		$E_{*H\#,D\#}^{act} = E_*^{act} + \Delta E^{H-D}$
30	*H#	+	*H#	$\rightarrow$	H_2	+	2*		$E_{*H\#,*H\#}^{act} = 2 \times E_*^{act}$
31	*H#	+	*D#	$\rightarrow$	HD	+	2*		$E_{*H\#,*D\#}^{act} = E_{*H\#,*H\#}^{act} + \Delta E^{H-D}$
32	H_2	+	*	$\rightarrow$	*H#	+	H#		$E_{H_2,*}^{diss} = 3481$ K (Diño et al. 2004)
33	HD	+	*	$\rightarrow$	*D#	+	H#		$E_{HD,*}^{diss} = E_{H_2,*}^{diss} + \Delta E^{H-D}$, 1/2 of the total dissociation rate
34	HD	+	*	$\rightarrow$	*H#	+	D#		$E_{HD,*}^{diss}$, 1/2 of the total dissociation rate

Notes. The energies are expressed in units of Kelvin. $\Delta E^{H-D} = 58$ K (5 meV), $\Delta E_{PAH}^{CH-CD} = 970$ K (83 meV), $\Delta E^{H_2-HD} = 415.8$ K .

**Table D.3.** Main gas-phase and singly-hydrogenated PAH reactions.

			Reaction				Comment
35		PAH	→	PAH#			Physisorption
36		PAH-H	→	PAH-H#			–
37		PAH–D	→	PAH-D#			–
38		PAH#	→	PAH			See Eq. (B.33)
39		PAH–H#	→	PAH-H			–
40		PAH–D#	→	PAH-D			–
41	PAH#	+ $h\nu$	→	PAH			Photodesorption
42	PAH–H#	+ $h\nu$	→	PAH-H			–
43	PAH–D#	+ $h\nu$	→	PAH-D			–
44	PAH#	+ CR	→	PAH			Cosmic-ray induced photodesorption
45	PAH–H#	+ CR	→	PAH-H			–
46	PAH–D#	+ CR	→	PAH-D			–
47	H	+ PAH	→	PAH-H			$E^{\mathrm{act}}_{\mathrm{PAH-H_x,H}} = 324$ K (Boschman et al. 2015)
48	D	+ PAH	→	PAH–D			$E^{\mathrm{act}}_{\mathrm{PAH-H_x,D}} = E^{\mathrm{act}}_{\mathrm{PAH-H_x,H}} + \Delta E^{\mathrm{H-D}}$, D-mass scaling of $1/\sqrt{2}$
49		PAH-H	→	H	+	PAH	Thermal H-detachment with $E^{\mathrm{b}}_{\mathrm{PAH-H}} = 16\,250$ K
50		PAH–D	→	D	+	PAH	$E^{\mathrm{b}}_{\mathrm{PAH-D}} = E^{\mathrm{b}}_{\mathrm{PAH-H}} + \Delta E^{\mathrm{CH-CD}}_{\mathrm{PAH}}$
51	PAH–H	+ $h\nu$	→	H	+	PAH	Photodetachment, $E(\mathrm{C-H}) = 1.4$ eV (16 250 K)
52	PAH–D	+ $h\nu$	→	D	+	PAH	$E(\mathrm{C-D}) = 4.367$ eV (50677.2 K)
53	PAH–H	+ H	→	H_2	+	PAH	$\sigma = 0.06$ Å^2/C atom, $E^{\mathrm{act}} = 0$ K $^{(a)}$
54	PAH–H	+ D	→	HD	+	PAH	Ten-fold H cross-section $\sigma = 0.06$–0.6 Å^2/C atom
55	PAH-D	+ H	→	HD	+	PAH	Same as for PAH–H
56	H	+ PAH^+	→	$\mathrm{PAH\text{-}H}^+$			$E^{\mathrm{act}}_{\mathrm{PAH-H_x^{n+},H}} = 116$ K
57	D	+ PAH^+	→	$\mathrm{PAH\text{-}D}^+$			$E^{\mathrm{act}}_{\mathrm{PAH-H_x^{n+},D}} = E^{\mathrm{act}}_{\mathrm{PAH-H_x^{n+},H}} + \Delta E^{\mathrm{H-D}}$
58	$\mathrm{PAH\text{-}H}^+$	+ e	→	PAH	+	H	Dissociative recombination
59	$\mathrm{PAH–D}^+$	+ e	→	PAH	+	D	–
60	$\mathrm{PAH–H}^+$	+ H	→	PAH^+	+	H_2	Langevin rate (Montillaud et al. 2013)
61	$\mathrm{PAH–H}^+$	+ D	→	PAH^+	+	HD	Same as for $\mathrm{PAH\text{-}H}^+$
62	$\mathrm{PAH–D}^+$	+ H	→	PAH^+	+	HD	Same as for $\mathrm{PAH\text{-}H}^+$
63	$\mathrm{PAH–H}^+$	+ HD	→	$\mathrm{PAH–D}^+$	+	H_2	
64	$\mathrm{PAH–D}^+$	+ H_2	→	$\mathrm{PAH–H}^+$	+	HD	Endothermic, $\Delta E^{\mathrm{reac}} = \Delta E^{\mathrm{H_2-HD}} - \Delta E^{\mathrm{CH-CD}}_{\mathrm{PAH}}$
65	H_2	+ PAH	→	PAH-H	+	H	$E^{\mathrm{diss}}_{\mathrm{H_2,PAH}}$–H–H = 3481 K
66	HD	+ PAH	→	PAH-D	+	H	$E^{\mathrm{diss}}_{\mathrm{HD,PAH}} = E^{\mathrm{diss}}_{\mathrm{H_2,PAH}} + \Delta E^{\mathrm{H_2-HD}}$
67	PAH	+ $h\nu$	→	PAH^+	+	e	Photoionisation
68	PAH	+ e	→	PAH^-			Electron attachment
69	PAH^-	+ $h\nu$	→	PAH	+	e	Photodetachement
70	PAH^+	+ e	→	PAH			Electron recombination
71	PAH^+	+ X	→	PAH	+	X^+	Charge exchange with species X
72	PAH	+ X^+	→	PAH^+	+	X	X = H and C, rates from Wolfire et al. (2008)
73	H	+ e^-	→	H^-	$h\nu$		Radiative attachment
74	D	+ e^-	→	D^-	$h\nu$		Radiative attachment
75	H	+ H^-	→	H_2	+	e^-	Associative detachment
76	H	+ D^-	→	HD	+	e^-	Associative detachment
77	D	+ H^-	→	HD	+	e^-	Associative detachment
78	H	+ D	→	HD	+	$h\nu$	Radiative association (Stancil & Dalgarno 1997)
79	H_2	+ D^+	→	HD	+	H^+	Honvault & Scribano (2013)
80	HD	+ H^+	→	H_2	+	D^+	$\Delta E^{\mathrm{reac}} = -416$ K
81	H_2	+ D	→	HD	+	H	Simbotin et al. (2011)
82	HD	+ H	→	H_2	+	D	$\Delta E^{\mathrm{reac}} = -416$ K
83	H + H	+ H	→	H_2	+	H	Three-body reactions
84	H + H	+ H_2	→	H_2	+	H_2	–
85	H_2	+ $h\nu$	→	H	+	H	Photodissociation including self-shielding
86	HD	+ $h\nu$	→	H	+	D	Photodissociation including self-shielding
87	H_2	+ CR	→	H	+	H	By secondary electrons and CR-generated UV photons
88	HD	+ CR	→	D	+	D	–

Notes. The energies are expressed in units of Kelvin. $\Delta E^{\mathrm{H-D}} = 58$ K (5 meV), $\Delta E^{\mathrm{CH-CD}}_{\mathrm{PAH}} = 970$ K (83 meV), $\Delta E^{\mathrm{H_2-HD}} = 415.8$ K.

References. $^{(a)}$Mennella et al. (2012); Rauls & Hornekær (2008).

Appendix E: Transmission function

Part of the difference in the H_2 formation efficiency can be explained by the choice of different transmission function. Figure E.1 shows the transmission function for α_{pc} using the Bell formulation or the transmission function in Cazaux & Tielens (2010). The Bell formulation gives a higher transmission in the quantum tunnelling part below 20 K while the exponential pre-factor in the Cazaux formulation is higher than the Bell pre-factor at high temperatures.
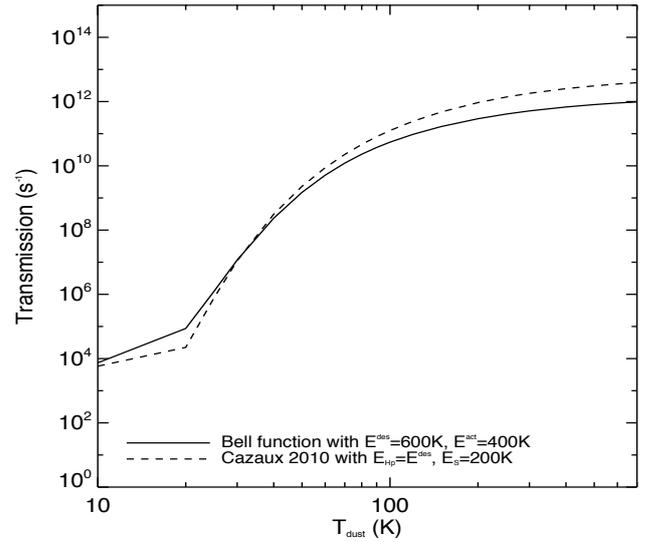
Fig. E.1. Transmission function α_{pc} using the Bell formulation or the formulation in Cazaux & Tielens (2010). The adopted values are given in the figure, the chosen value for the quantum width is 2.5 Å for silicate.

Appendix F: Tables of variable symbols

The main variable symbols are summarised in Tables F.1.

Table F.1. Variables used in the manuscript.

Variable	Symbol	Units and remarks
Species i mass	m_i	gram
Dust grain radius squared	r^2	cm^2, input parameter
Dust number density	$n_{\rm d}$	cm^{-3}
Number density of gas-phase species i	n_i	cm^{-3}
Surface density of adsorption sites	$N_{\rm surf}$	1.5×10^{15} cm^{-2}, input parameter
Number of adsorption sites per ice monolayer	$nb_{\rm site}$	no units, $nb_{\rm site} = 4\pi N_{\rm surf} r^2$
Surface site cross-section	$\sigma_{\rm surf,site}$	$\sigma_{\rm surf,site} = 1/N_{\rm surf}$ cm^2
Total number density of chemisorption sites	$n_{\rm surf,chem}$	$n_{\rm surf,chem} = nb_{\rm site} n_{\rm d} = 4\pi N_{\rm surf} r^2 n_{\rm d}$ cm^{-3}
Number density of physisorbed species i	$n_{\#,i}$	cm^{-3}
Number density of chemisorbed species i	$n_{*,i}$	cm^{-3}
Number density of unoccupied chemisorption sites	n_*	$n_* = n_{\rm surf,chem} - \sum_i n_{*,i}$ cm^{-3}
Number density of chemically active physisorbed species i	$n_i^{\rm act}$	cm^{-3}
Number of chemically active physisorption layers	$N_{\rm act}$	no units, an input parameter with typical value 1–10
Total number of density of physisorbed species (ice)	$n_{\#,\rm tot}$	$n_{\#,\rm tot} = \sum_i n_{\#,i}$ cm^{-3}
Number of physisorbed ice layers per grain	$N_{\rm layer}$	no units, $N_{\rm layer} = n_{\#,\rm tot}/(n_{\rm d}\, nb_{\rm site})$
Fraction of available adsorption sites	$f_{\rm avail}$	1 for physisorption for chemisorption $= n_*/n_{\rm surf,chem}$ if $N_{\rm layer} < 1, = 0$ if $N_{\rm layer} \geqslant 1$
Gas temperature	$T_{\rm g}$	K
Dust temperature	$T_{\rm d}$	K
General activation barrier width	$a_{\rm Å}$	Å
Activation barrier	$E_{\rm act}$	K
Species mass in atomic mass units	$m_{\rm amu}$	amu
General adsorption rate	$R_i^{\rm ads}$	s^{-1}
General sticking coefficient	S_i	no units, between 0 and 1
General Bell's formula	$Q_{\rm Bell}$	no units
Physisorption rate	$R_i^{\rm gp}$	s^{-1}
Physisorption sticking coefficient	$S_{\rm phys}$	no units, between 0 and 1
Species i thermal speed	$v_i^{\rm th}$	cm s^{-1}
Chemisorption activation energy	$E_i^{\rm gc}$	erg
Chemisorption rate	$R_i^{\rm gc}$	s^{-1}
Chemisorption Bell's function	$Q_i^{\rm gc}$	no units
Chemisorption sticking coefficient	$S_{\rm chem}$	no units, between 0 and 1
Chemisorption activation barrier width	$a_i^{\rm gc}$	cm, assuming a rectangular-shaped barrier
Desorption energy	$E_i^{\rm des}$	erg
Binding energy	$E_i^{\rm b}$	erg, physisorption and chemisorption
Desorption activation energy	$E_i^{\rm des,act}$	erg, non-null for desorption from chemisorption sites
Surface vibration frequency	$\nu_{0,i}$	$\nu_{0,i} = \sqrt{(2N_{\rm surf} E_i^{\rm b})/(\pi^2 m_i)}$ Hz
Activation barrier for desorption	$E_i^{\rm des,act}$	erg, non null for chemisorption
Desorption energy	$E_i^{\rm des}$	erg, for either the physisorbed ($=E_i^{\rm b}$) chemisorbed ($=E_i^{\rm b} + E_i^{\rm des,act}$)
Total desorption rate from a physisorption site	$R_i^{\rm des,pg}$	s^{-1}
Thermal desorption rate from a physisorption site	$R_i^{\rm pg,th}$	s^{-1}
Photodesorption rate from a physisorption site	$R_i^{\rm pg,ph}$	s^{-1}
Photodesorption yield	Y_i	no units
UV flux enhancement w.r.t. to the ISM value	$\chi F_{\rm Draine}$	$1\,\chi F_{\rm Draine} = 1.9921 \times 10^8$ photons cm^{-2} s^{-1}
Cosmic-Ray induced desorption rate from a physisorption site	$R_i^{\rm pg,CR}$	s^{-1}
Activation barrier width for desorption from a chemisorption site	$a_i^{\rm des,act}$	cm
Total desorption rate from a chemisorption site	$R_i^{\rm des,cg}$	s^{-1}
Thermal desorption from a chemisorption site	$R_i^{\rm cg,th}$	s^{-1}
Photodesorption rate from a chemisorption site	$R_i^{\rm cg,ph}$	s^{-1}
Cosmic-ray induced desorption from a chemisorption site	$R_i^{\rm cg,CR}$	$\simeq 0$ s^{-1}
Fraction of time a grain remains at 70 K up upon a cosmic-ray hit	$f(70K)$	no units
Thermal desorption rate for a dust grain at 70 K	$R_i^{\rm pg,th}(70K)$	s^{-1}
Thermal diffusion rate for a dust grain at 70 K	$R_i^{\rm diff,th}(70K)$	s^{-1}
Thermal surface diffusion rate	$R_i^{\rm diff,th}$	s^{-1}, includes quantum tunnelling effect
Cosmic-Ray induced surface diffusion rate	$R_i^{\rm diff,CR}$	s^{-1}
Bell's formula for the diffusion processes	$Q_i^{\rm diff}$	no units

Notes. The index i means that the variable applies to species i. Depending on the process, the species i is a gas-phase, physisorbed, or chemisorbed species.

Table F.1. continued.

Variable	Symbol	Units and remarks
Diffusion activation energy	E_i^{diff}	erg
Diffusion activation barrier width	a_i^{diff}	cm
Total surface diffusion rate	R_i^{diff}	$R_i^{\text{diff}} = R_i^{\text{diff,th}} + R_i^{\text{diff,CR}}$ s^{-1}, $P_i^{\text{diff}} = R_i^{\text{diff}}/\nu_{0,i}$
Activation barrier width for diffusion	a_i^{diff}	cm
Hydrogen diffusion barrier between physisorption sites	$E_{\text{H}\#}^{\text{diff}}$	erg
Hydrogen diffusion barrier between chemisorption sites	$E_{*\text{H}\#}^{\text{diff}}$	erg
Deuterium diffusion barrier between physisorption sites	$E_{\text{D}\#}^{\text{diff}}$	erg
Deuterium diffusion barrier between chemisorption sites	$E_{*\text{D}\#}^{\text{diff}}$	erg
Physisorbed hydrogen desorption energy	$E_{\text{p}}^{\text{des}}$	erg
Physisorbed deuterium desorption energy	$E_{\text{D}_{\text{p}}}^{\text{des}}$	erg
Chemisorbed hydrogen desorption energy	$E_{\text{c}}^{\text{des}}$	erg
Chemisorbed deuterium desorption energy	$E_{\text{c}}^{\text{des}}$	erg
Surface reaction rate coefficient between species i and j	k_{ij}	cm^3 s^{-1}
Surface reaction probability	κ_{ij}	no units, between 0 and 1
Surface reaction activation barrier	E_i^{act}	erg
Surface reaction activation barrier width	a_{ij}^r	cm
Hydrogen thermal desorption rate from a physisorption site	$R_{\text{H}\#}^{\text{pg}}$	s^{-1}
Hydrogen diffusion rate between physisorption sites	$R_{\text{H}\#}^{\text{diff}}$	s^{-1}
Hydrogen transfer rate from a physisorption to a chemisorption site	$R_{\text{H}\#}^{\text{pc}}$	s^{-1}
Activation barrier energy for H transfer from a physisorption to a chemisorption site	$E_{\text{H}\#}^{\text{act}}$	erg
Bell's function for H transfer from a physisorption to a chemisorption site	$Q_{\text{H}\#}^{\text{pc}}$	no units
Hydrogen transfer rate from a chemisorption to a physisorption site	$R_{*\text{H}\#}^{\text{cp}}$	s^{-1}
Eley-Rideal H$_2$ formation rate (physisorption site)	$R_{\text{H}_2}^{\text{gp}}$	s^{-1}
Eley-Rideal H$_2$ formation rate (chemisorption site)	$R_{\text{H}_2}^{\text{gc}}$	s^{-1}
H$_2$ formation rate after encounter between a physisorbed and a chemisorption H-atom	$R_{\text{H}\#,*\text{H}\#}$	cm^3 s^{-1}
PAH effective radius	a_{PAH}	cm
PAH number of carbon atoms	N_{C}	no units
PAH number of hydrogen atoms	N_H	no units
PAH ionisation potential	IP_{PAH}	erg
Hydrogenated PAH hydrogen association rate coefficient	$k_{\text{PAH}-\text{H}_x,\text{H}}$	cm^3 s^{-1}
Hydrogen association on PAH-H$_x$ activation energy	$E_{\text{PAH}-\text{H}_x,\text{H}}^{\text{act}}$	erg
Hydrogenated PAH hydrogen abstraction rate coefficient	$k_{\text{PAH}-\text{H}_x}$	cm^3 s^{-1}
Effective temperature upon absorption of a photon of energy $h\nu$	T_e	K
PAH internal temperature	T_{PAH}	K
Unimolecular PAH thermal dissociation rate at T_e	$R_{\text{PAH}-\text{H}_x,T_e}$	s^{-1}
Hydrogen binding energy on PAH-H$_x$	E_0	erg, $\sim$1–2 eV
Yield for PAH-H$_x$ photodissociation	$Y_{\text{PAH}-\text{H}_x,\text{UV}}$	no units, $= 0$ for $h\nu < E_0$
Typical PAH IR photon emission rate	R_{IR}	$\sim$1 s^{-1}
Thermal unimolecular dissociation rate	$R_{\text{PAH}-\text{H}_x,\text{therm}}$	s^{-1}
Hydrogen association rate coefficient for (hydrogenated) PAHs cations	$k_{\text{PAH}-\text{H}_x^{n+},\text{H}}$	cm^3 s^{-1}
Activation energy for hydrogen association for PAH cations	$E_{\text{PAH}-\text{H}_x^{n+},\text{H}}^{\text{act}}$	erg
Hydrogenated ionised PAH hydrogen abstraction rate coefficient	$k_{(\text{PAH}-\text{H}_x)^{n+}}$	cm^3 s^{-1}
Energetic particle induced photoionisation rate coefficient	$k_{\text{pi,MeV}}$	cm^3 s^{-1}
Energetic particle induced photodetachment rate coefficient	$k_{\text{pd,CR}}$	cm^3 s^{-1}
Singly-ionised PAH cations electron recombination rate coefficient	k_{er}	cm^3 s^{-1}
Multiply-ionised PAH cations electron recombination rate coefficient	k_{er}'	cm^3 s^{-1}
PAH shape correction factor	ϕ_{PAH}	$\phi_{\text{PAH}} = \sigma_{\text{disk}}/\sigma_{\text{sphere}}$
PAH electron attachment rate coefficient	k_{ea}	cm^3 s^{-1}
Electron sticking coefficient on PAHs	$S_{\text{PAH}}(e^-)$	no units
Mutual neutralisation rate coefficient	k_{mn}	cm^3 s^{-1}
Electron collisional detachment rate coefficient	k_{nd}	cm^3 s^{-1}
Neutral PAH charge-exchange reactions	$k_{\text{ce,0}}$	cm^3 s^{-1}
Charged PAH charge-exchange reactions	$k_{\text{ce,n}}$	cm^3 s^{-1}
Double charge transfer reaction	k_{di}	cm^3 s^{-1}
PAH adsorption/desorption energy	$E_{\text{PAH,des}}$	cm^3 s^{-1}
Total H$_2$ formation rate according to Cazaux & Tielens (2002, 2004)	$R_{\text{H}_2}^{\text{Cazaux}}$	s^{-1}
H$_2$ recombination efficiency	ϵ	Cazaux & Tielens (2002)
Total H$_2$ formation rate according to Jura (1974, 1975a,b)	$R_{\text{H}_2}^{\text{Jura}}$	s^{-1}